



# Deep Ultraviolet, Emission-line Imaging of the Makani Galactic Wind

Triet Ha<sup>1</sup>, David S. N. Rupke<sup>1,2</sup>, Shane Caraker<sup>1</sup>, Jack Harper<sup>1</sup>, Alison L. Coil<sup>3</sup>, Miao Li<sup>4</sup>, Christy A. Tremonti<sup>5</sup>, Aleksandar M. Diamond-Stanic<sup>6</sup>, James E. Geach<sup>7</sup>, Ryan C. Hickox<sup>8</sup>, Sean D. Johnson<sup>9</sup>, Gene C. K. Leung<sup>10</sup>, John Moustakas<sup>11</sup>, Serena Perrotta<sup>3</sup>, Gregory H. Rudnick<sup>12</sup>, Paul H. Sell<sup>13</sup>, and Kelly E. Whalen<sup>14</sup>

<sup>1</sup>Department of Physics, Rhodes College, 2000 N. Parkway, Memphis, TN 38104, USA; [drupke@gmail.com](mailto:drupke@gmail.com)

<sup>2</sup>Zentrum für Astronomie der Universität Heidelberg, Astronomisches Rechen-Institut, Mönchhofstr 12-14, D-69120 Heidelberg, Germany

<sup>3</sup>Department of Astronomy and Astrophysics, University of California, San Diego, La Jolla, CA 92093, USA

<sup>4</sup>Flatiron Institute, Center for Computational Astrophysics, New York, NY 10010, USA

<sup>5</sup>Department of Astronomy, University of Wisconsin-Madison, Madison, WI 53706, USA

<sup>6</sup>Department of Physics and Astronomy, Bates College, Lewiston, ME 04240, USA

<sup>7</sup>Centre for Astrophysics Research, University of Hertfordshire, Hatfield, Hertfordshire AL10 9AB, UK

<sup>8</sup>Department of Physics and Astronomy, Dartmouth College, Hanover, NH 03755, USA

<sup>9</sup>Department of Astronomy, University of Michigan, 1085 S. University, Ann Arbor, MI 48109, USA

<sup>10</sup>MIT Kavli Institute for Astrophysics and Space Research, 77 Massachusetts Ave., Cambridge, MA 02139, USA

<sup>11</sup>Department of Physics and Astronomy, Siena College, Loudonville, NY 12211, USA

<sup>12</sup>Department of Physics and Astronomy, University of Kansas, Lawrence, KS 66045, USA

<sup>13</sup>Department of Astronomy, University of Florida, Gainesville, FL 32611, USA

<sup>14</sup>NASA Goddard Space Flight Center, Code 662, Greenbelt, MD 20771, USA

Received 2024 December 21; revised 2025 April 2; accepted 2025 April 7; published 2025 June 9

## Abstract

The O VI 1032, 1038 Å line is a key probe of cooling gas in the circumgalactic medium (CGM) of galaxies but has been observed to date primarily in absorption along single sight lines. We present deep Hubble Space Telescope (HST) Solar Blind Channel of the Advanced Camera for Surveys observations of the compact, massive starburst Makani. Makani hosts a 100 kpc, [O II]-emitting galactic wind driven by two episodes of star formation over 400 Myr. We detect O VI and Ly $\alpha$  emission across the [O II] nebula with similar morphology and extent, out to  $r \approx 50$  kpc. Using differential narrowband imaging, we separate Ly $\alpha$  and O VI and show that the O VI emission is comparable in brightness to [O II], with  $L_{\text{O VI}} = 4 \times 10^{42} \text{ erg s}^{-1}$ . The similar hourglass morphology and size of [O II] and O VI implicate radiative cooling at  $T = 10^{5.5} \text{ K}$  in a hot–cold interface. This may occur as the  $T > 10^7 \text{ K}$  CGM—or the hot fluid driving the wind—exchanges mass with the  $T \approx 10^4 \text{ K}$  clouds entrained in (or formed by) the wind. The optical/UV line ratios may be consistent with shock ionization, although uncertain attenuation and Ly $\alpha$  radiative transfer complicate the interpretation. The detection of O VI in Makani lies at the bleeding edge of the UV imaging capabilities of HST and provides a benchmark for future emission-line imaging of the CGM with a wide-area UV telescope.

*Unified Astronomy Thesaurus concepts:* Circumgalactic medium (1879); Starburst galaxies (1570); Galaxy winds (626)

## 1. Introduction

The circumgalactic medium (CGM) surrounds galaxies and fills their virial halos with hot, diffuse, and metal-enriched gas. These metals are ejected by galactic winds from central and satellite galaxies (T. M. Tripp et al. 2011; Z. Hafen et al. 2019). The CGM likely contains the majority of metals produced in galaxies (J. Tumlinson et al. 2011; J. K. Werk et al. 2014).

Much of the mass in the CGM may reside in a warm-hot phase that traces cooling gas (J. K. Werk et al. 2014). A key tracer of this phase is O VI 1031.912, 1037.613 Å in absorption, whose emissivity peaks in a narrow range around  $T \approx 10^{5.5} \text{ K}$  (R. S. Sutherland & M. A. Dopita 1993). Quasars or galaxies back illuminate the CGM of galaxies that are nearby in projection. The statistical analysis of O VI absorbers shows that they are most common around actively star-forming galaxies (J. Tumlinson et al. 2011; K. Tchernyshyov et al. 2023), suggesting a connection between the ionization state of oxygen in the CGM and the feedback process.

Imaging the CGM in emission is much more challenging, as many of the expected line coolants lie in the UV and X-ray

bands (S. Bertone et al. 2013). O VI 1032, 1038 Å is one of the most observable of these—due to its brightness and that it arises conveniently in wavelength near Ly $\alpha$ —despite it not being the dominant ionization state of oxygen in the CGM (B. D. Oppenheimer et al. 2016). Presently, deep, narrowband observations are still required to image extended O VI. Current UV-sensitive telescopes (primarily the Hubble Space Telescope [HST]) are hard-pressed to meet the sensitivity required to detect the diffuse, low-surface-brightness emission that is expected.

Using two Far Ultraviolet Spectroscopic Explorer (FUSE) spectra, B. Otte et al. (2003) were the first to detect O VI in emission from a spiral galaxy other than the Milky Way. The O VI emission in NGC 4631 has a scale height of 8 kpc and is coincident with an outflowing, X-ray-emitting bubble along the galaxy minor axis. Weak O VI emission was later detected with FUSE in integrated spectra of nearby star-forming galaxies (J. P. Grimes et al. 2007, 2009).

A synthetic narrowband imaging technique was successfully deployed by M. Hayes et al. (2016) to image the O VI emission surrounding the nearby galaxy SDSS J115630.63+500822.1 (hereafter J1156) using the Solar Blind Channel of the Advanced Camera for Surveys (ACS-SBC) aboard HST. They detect O VI emission out to 23 kpc in an exponential halo with scale length  $r_{\text{exp}} = 7.5 \text{ kpc}$  and luminosity  $L_{\text{O VI}} = 2 \times 10^{41} \text{ erg s}^{-1}$ . By comparing to column densities measured in absorption,

M. Hayes et al. (2016) infer that the emission arises from the interface between hot gas and small ( $<10$  pc), cool clouds (see also J. Chisholm et al. 2018) in a starburst-driven galactic wind.

The giant Makani nebula is one of the first examples of a galactic wind that is directly observed to be moving well into the CGM of its host (D. S. N. Rupke et al. 2019). The nebula was detected in the light of [O II] 3727, 3729 Å and has an observed luminosity of  $L([\text{O II}]) = 3.3 \times 10^{42} \text{ erg s}^{-1}$ . Its radius is 50 kpc, which is 25 times the stellar half-light radius of the host galaxy. The hourglass morphology and gas kinematics indicate the nebula arises from an outflow. The host galaxy—SDSS J211824.06+001729.4, aka Makani—is a  $z = 0.4590$ ,  $M_* = 10^{11} M_\odot$  merger remnant hosting a compact starburst (P. H. Sell et al. 2014; A. M. Diamond-Stanic et al. 2021). With a star formation rate (SFR) of 225–300  $M_\odot \text{ yr}^{-1}$  (G. C. Petter et al. 2020) and a fast wind with  $(dM/dt)/\text{SFR} \sim 1$  (S. Perrotta et al. 2021; D. S. N. Rupke et al. 2023), it is a likely example of an Eddington-limited starburst (A. M. Diamond-Stanic et al. 2012).

The wind consists of a two-stage flow. First, a  $\langle\sigma\rangle = 200 \text{ km s}^{-1}$  ionized outflow at radii 20–50 kpc emerged from a starburst  $\approx 400$  My in the past (episode I). Second, a  $\langle\sigma\rangle = 400 \text{ km s}^{-1}$ , neutral/molecular/ionized flow—with velocities up to 2000  $\text{km s}^{-1}$ —was driven out to 10–20 kpc by a recent burst of age 7 Myr (episode II). Makani is part of a sample of mergers (P. H. Sell et al. 2014) that may be progressing through a brief stage (K. E. Whalen et al. 2022) of stellar mass buildup (A. M. Diamond-Stanic et al. 2021) driven by starbursts that power high-velocity (J. D. Davis et al. 2023), massive (S. Perrotta et al. 2023) outflows.

The size and brightness of the Makani oxygen nebula make it a prime candidate for imaging O VI in a galactic wind as it interacts with the CGM. The rest-frame optical lines and molecular gas emission are consistent with a massive ( $10^{10} M_\odot$ ), shock-ionized wind (D. S. N. Rupke et al. 2019, 2023). M. Hayes et al. (2016) find that the coronal, O VI-emitting gas in J1156 arises at much larger scales than the compact, photoionized line emission. Determining where the O VI arises in Makani, and its relationship to the line emission from lower-ionization gas, will inform our understanding of the relationship between cold clouds in a wind and the hot gas in which they are embedded. This interaction is a subject of intense interest, as it impacts our understanding of the origin and fate of the clouds driven in a galactic wind and the redistribution of gas and metals into the CGM (D. B. Fielding & G. L. Bryan 2022).

In Section 2 we lay out the observations and data reduction. In Section 3 we present the resulting observed morphology, interpret the source of the observed emission, and compute line fluxes. Finally, we compare to simulations and models in Section 4. Throughout we take as systemic the stellar redshift of Makani,  $z = 0.4590$  (D. S. N. Rupke et al. 2019), and assume a flat  $\Lambda$  cosmology with  $\Omega_m = 0.315$  and  $H_0 = 67.4 \text{ km s}^{-1} \text{ Mpc}^{-1}$  (Planck Collaboration et al. 2020). This results in a projected physical scale of 6.02 kpc  $\text{arcsec}^{-1}$  at the distance of Makani. The vacuum rest wavelengths of the lines of interest in this paper are 1031.912 Å (O VI 1032 Å), 1037.613 Å (O VI 1038 Å), and 1215.6701 Å (Ly $\alpha$ ).

## 2. Observations and Data Reduction

### 2.1. Observations with HST

We imaged Makani with the ACS-SBC (H. D. Tran et al. 2003; M. Sirianni et al. 2005) on HST as part of a Cycle 28

program (PID 16231, PI Rupke). We observed Makani through the F150LP and F165LP long-pass UV filters.

F150LP passes wavelengths above  $\approx 1450$  Å (STScI Development Team 2018, 2020; J. E. Ryon et al. 2023), with a blue leak of throughput  $\mathcal{T} < 0.1\%$  down to 1420 Å and a tail to longer wavelengths that dips below  $\mathcal{T} = 0.01\%$  at 2000 Å. Figure 1 illustrates the proximity of redshifted O VI wavelengths (1505 and 1514 Å) to the wavelength of the peak of the system throughput for F150LP, 1490 Å. The throughput at redshifted O VI is 3.8%–3.9%, compared to  $\mathcal{T} = 4.1\%$  at the filter peak. This is why Makani and F150LP are well-matched for this experiment, despite the overall low system throughput at these wavelengths.

F150LP also includes redshifted Ly $\beta$  and Ly $\alpha$  at 1497 and 1774 Å. We expect Ly $\beta$  to be weak, as we discuss in Section 4. The throughput at Ly $\alpha$  is  $\mathcal{T} = 0.79\%$ , or about 5 times smaller than the throughput near redshifted O VI. Ly $\alpha$  is nonetheless a strong line and could contaminate any measurement with F150LP alone.

F165LP passes wavelengths above  $\approx 1600$  Å, with a peak throughput of  $\mathcal{T} = 1.1\%$  at 1700 Å and a tail to longer wavelengths. F165LP thus includes Ly $\alpha$ , as well, but crucially not O VI. F165LP looks much like F150LP but with a higher low-wavelength cutoff. Notably,  $\mathcal{T}_{\text{F150LP}} - \mathcal{T}_{\text{F165LP}} < 0.1\%$  at wavelengths above 1750 Å. The difference of these two filters thus cleanly includes O VI but not Ly $\alpha$ . The percentage difference between the filters at redshifted Ly $\alpha$  is only  $\Delta\mathcal{T}/\mathcal{T} = 7\%$ . Thus, if O VI and Ly $\alpha$  were equal in flux in Makani and no other lines were present, an image created by subtracting F165LP directly from F150LP would in principle contain residual Ly $\alpha$  at 2% of the flux of O VI. Neither filter contains strong geocoronal lines or significant amounts of earthshine or zodiacal light (J. E. Ryon et al. 2023).

We planned 20 orbits to reach a total exposure time of  $\approx 25,000$  s per filter. We grouped these into 10 visits of 2 orbits each. In each orbit we observed the galaxy in either the F150LP or F165LP filter in a multiple of the default four-point box dither to subsample at the 1/2 pixel level. (We expanded the default dither by a factor of 5 to prevent overlap of the bad anode—the central blank strip of six rows (J. E. Ryon et al. 2023)—among exposures.) In the second orbit of each visit, we switched filters and repeated the four-point dither. At each dither step we exposed for 624 s in orbit 1 and 626–627 s in orbit 2. We alternated the first filter to be observed from visit to visit. This results in four exposures per filter per visit, for a total exposure time per visit of 2496–2508 s in each filter.

The most significant noise source for the ACS-SBC MAMA detector, aside from photon statistics, is the dark current. For detector temperatures below  $\approx 25^\circ\text{C}$ , the dark current is relatively stable at  $1 \times 10^{-5} \text{ counts s}^{-1} \text{ pixel}^{-1}$  (C. Cox 2009; R. J. Avila 2017). However, once the detector is powered on, its temperature increases with time—reaching  $>25^\circ\text{C}$  after  $\approx 2$  hr (R. J. Avila 2017)—which in turn causes the dark current to rise (C. Cox 2009). Furthermore, there is a region of high dark current in a large, off-center “halo” on the detector. Thus, recommended practice is to limit ACS-SBC visits to 1–2 orbits, to keep ACS-SBC visits separated by at least 24 hr, and to place targets near the corner of the detector with lowest dark current (R. J. Avila et al. 2018). The dark current remains relatively stable and low in this region at  $T < 25^\circ\text{C}$ , even at recent times (A. M. Guzman & R. J. Avila 2024).

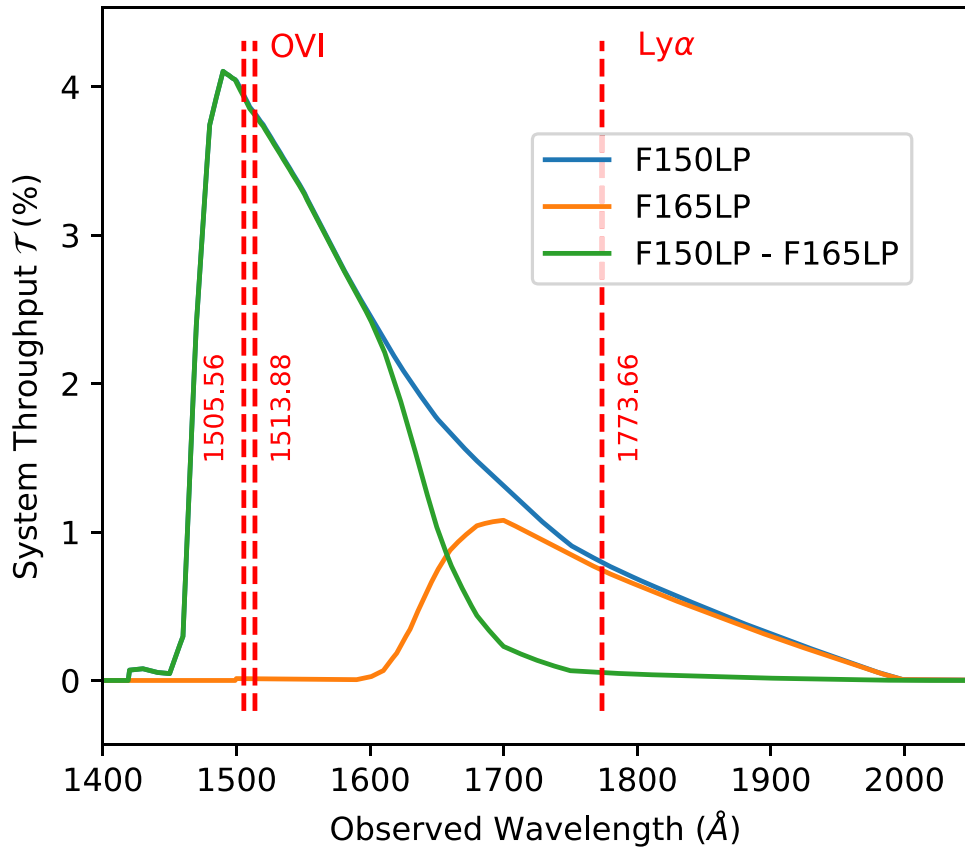


**Figure 1.** System throughputs for the ACS-SBC F150LP and F165LP filters through which we imaged Makani (STScI Development Team 2018, 2020; J. E. Ryon et al. 2023), shown as blue and orange lines; their difference is in green. The wavelengths of O VI and Ly $\alpha$  are marked as vertical red dashed lines and labeled with their expected wavelengths in the observed frame. The difference of the two filters includes O VI emission but minimal Ly $\alpha$ .

We followed the first two of these recommendations. Our visits were limited to two orbits, and we requested the ACS-SBC be switched off at least 24 hr between visits. Centering in the low-dark region was impossible, however. The long axis of the Makani nebula is  $17''$  in size, whereas the detector field of view (FOV) is  $34''.6 \times 30''.5$ . Furthermore, we dithered in a nine-point box pattern between visits—using a  $\approx 3''.2$  step size in each dimension—to average over low-frequency flat-field variations. We also did not specify the HST roll angle, to maximize scheduling flexibility. Because we did not specify a particular orientation, the actual visit-to-visit grid rotated over time.

These constraints meant that the galaxy was typically positioned somewhere between the nominal SBC-LODARK aperture (R. J. Avila et al. 2018) and the detector center. However, we did shift the observing center toward the SBC-LODARK aperture as much as possible, while ensuring the full nebula would remain in the FOV.

In practice, a series of issues required multiple reobservations. The originally planned visits are labeled 01–10. (1) Visits 02 and 05 failed due to HST safing in 2021 June. These were replaced by visits 52 and 55. (2) These visits were scheduled but did not occur due to a second safing in 2021 October. Visits 52 and 55 were then replaced by visits 56 and 57. (3) Three orbits acquired no data due to failure of guide star reacquisition: orbit 2 of visits 06, 07, and 59 (see below). Orbit 2 of visits 06 and 07 was replaced with visit 58. Orbit 2 of visit 59 was not repeated. (4) Visit 09 was scheduled directly after visit 08, so the dark current continued to increase

and the noise in these data is high. (Visit 10 also occurred 19 hr after visit 09—less than the optimal 24 hr—but the data are not severely impacted.) Visit 59 was implemented to replace visit 09.

## 2.2. Data Reduction

We retrieved 96 flat-fielded exposures—the `flt.fits` files—from MAST (DOI:10.17909/x1eh-rb90). Removing 12 with no data (orbit 2 of three visits in which guide star reacquisition failed) leaves 84 total exposures, for a total exposure time of 52,500 s.

We investigated the relationship between the dark current  $D_{300}$  and the detector temperature  $T_{\text{det}}$  for each flat-fielded exposure (Figure 2). We approximated  $T_{\text{det}}$  as the average values of the temperatures measured before and after the exposure, recorded in the header keywords `MDECODT1` and `MDECODT2`. The data were converted to units of electrons during the flat-field correction process (R. A. Lucas et al. 2022). For each file, we used its DQ array to exclude low-quality pixels and divided the data by the exposure time  $t_{\text{exp}}$  obtained from the header keyword `EXPTIME`. These steps followed the methods discussed in A. M. Guzman & R. J. Avila (2024). We computed the dark level  $D_{300}$  for each image by averaging pixel values within a  $300 \text{ pixel} \times 300 \text{ pixel}$  square centered on the pixel (567, 561) while excluding a  $100 \text{ pixel} \times 100 \text{ pixel}$  square around the galaxy center. This method ensured that the dark current measurement included the information from the regions of highest dark current while avoiding the galaxy

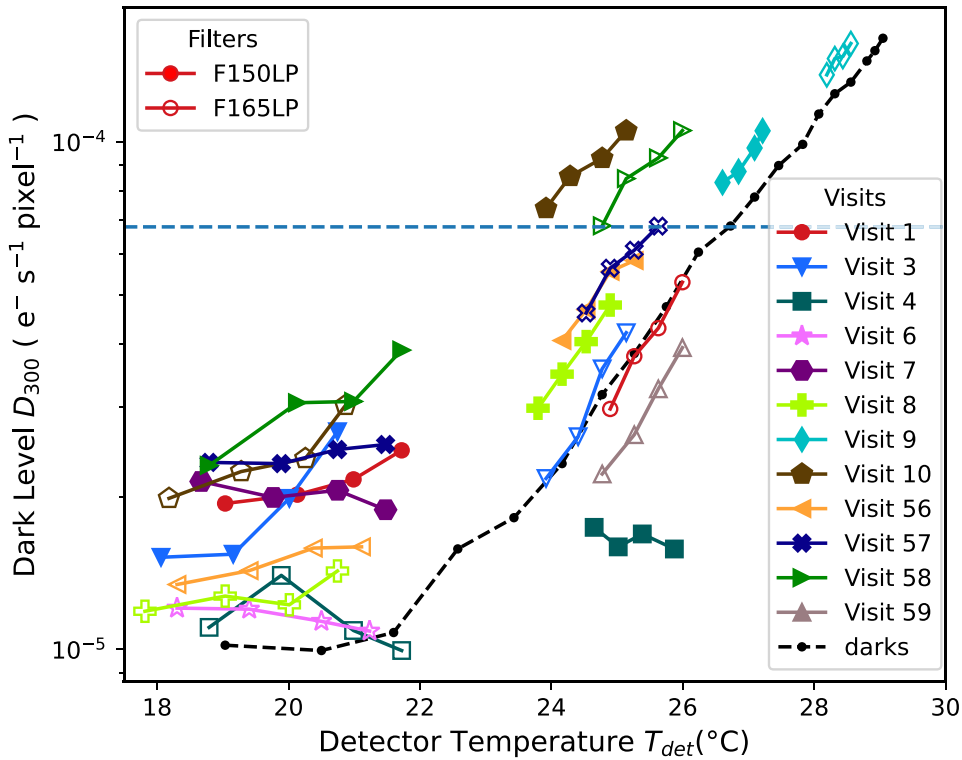


**Figure 2.** The relationship between the average dark level  $D_{300}$  and the detector temperature  $T_{det}$ .  $D_{300}$  is calculated in a  $300 \text{ pixel} \times 300 \text{ pixel}$  box near the detector center, with the galaxy masked. The solid (empty) colored dots represent single flat-fielded exposures collected with the filter F150LP (F165LP). Different symbols denote different visits. The black dots represent data taken in 2022 with the camera shutter closed. Our data follow the 2022 dark pattern of increasing dark with increasing temperature above  $\approx 20^\circ\text{C}$ , but with a varying normalization. The horizontal blue dashed line represents the cutoff used to eliminate data points with significantly high dark levels.

itself and the lowest dark current near the field edges. We retained  $D_{300}$  to weight each image during registration.

At low temperatures ( $T_{det} < 24^\circ\text{C}$ ), the dark current was uniformly flat at less than  $4 \times 10^{-5} \text{ counts s}^{-1} \text{ pixel}^{-1}$ . As the temperature rose, the dark level rose and the off-center halo became more prominent. This trend was discussed extensively in the previous ACS-SBC dark rate reports (C. Cox 2009; R. J. Avila 2017; A. M. Guzman & R. J. Avila 2024). For comparison, we downloaded 20 SBC precalibrated dark images collected in 2022 March (PID 16529, PI Robert Avila). These 1000 s exposures were used by the ACS Team to monitor the dark rate of ACS-SBC and how it changed over time (A. M. Guzman & R. J. Avila 2024). We performed CALACS calibration on these exposures to the point of flat-fielded correction. For each processed dark image, we computed the dark level per pixel, excluding bad-quality pixels flagged by the DQ array and normalizing with the exposure time. We plot their dark levels versus the corresponding detector temperatures in Figure 2.

Using these dark measurements, we eliminated two orbits in each filter with significantly high dark levels: visit 09 orbit 1 and visit 10 orbit 2 for F150LP; and visit 09 orbit 2 and visit 58 orbit 2 for F165LP. This cut left 36 exposures in F150LP and 32 in F165LP.

Prior to image registration, we corrected the shifts in coordinate zero-points caused by the use of different guiding stars in different visits. To do this, we adjusted the World Coordinate System (WCS) information in each exposure, matching the galaxy’s centroid coordinate in each exposure with a reference coordinate.

We drizzled images from the same filter onto a common grid using *DrizzlePac* (STScI Development Team 2012). We passed our data to *astrodrizzle*, choosing an output plate scale of  $0''.2914 \text{ pixel}^{-1}$  to match the KCWI [O II] image for a direct comparison. Since the output pixels are 9 times bigger than the SBC detector pixels in each dimension, the pixel drop size, determined by the `final_pixfrac` parameter, does not significantly affect the final image. Therefore, we chose `final_pixfrac=1` to minimize dark noise. During drizzling, we weighted each image by the ratio of its exposure time and dark level,  $t_{exp}/D_{300}$  (H. I. Teplitz et al. 2006). We carried out the weighting process by first dividing each image and its exposure time by the dark level computed previously. Then we combined these adjusted images with *astrodrizzle*, setting the parameter `final_wht_type=EXP`.

We obtained the variance map by passing the unweighted flat-fielded and WCS-shifted data again to *astrodrizzle*, but this time with `final_wht_type = ERR`. When individual exposures are processed, CALACS computes the noise  $N$  from the signal  $S$  as  $N = \max(1, \sqrt{S})$ , which accounts for the fact that most pixels record 0 counts (R. A. Lucas et al. 2022). Since we drizzle to much larger pixels, this resulted in an overestimate of the drizzled variance by a factor equal to the ratio of the original and drizzled pixel areas, which in this case was  $\approx 83$ . We correct the variance map for this effect.

Finally, we computed the photometric centroid of each drizzled image and assigned to it a reference coordinate. To compute the reference coordinate, we downloaded the HST-WFC3 F814W image (P. H. Sell et al. 2014), as reprocessed using the Hubble Advanced Pipeline Single-Visit Mosaics and aligned to Gaia DR3. We applied

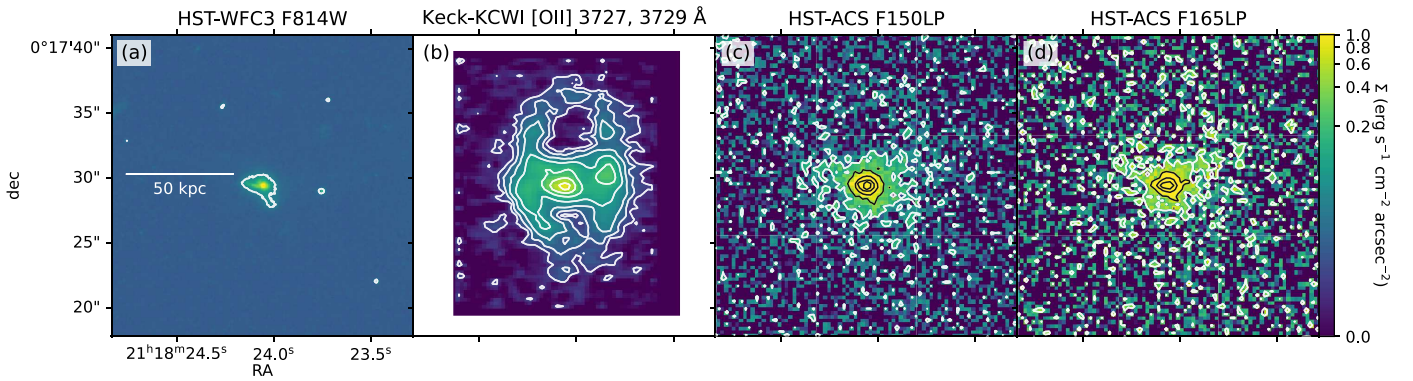


**Figure 3.** HST optical, Keck [O II], and HST UV images. (a) HST-WFC3 F814W image (P. H. Sell et al. 2014). The contour is  $0.5 e^- \text{ pixel}^{-1}$ . The compact size of the galaxy is evident; half of the starlight is concentrated within a 2 kpc radius. (b) Makani in the light of [O II] 3727, 3729 Å, as observed with Keck-KCWI (D. S. N. Rupke et al. 2019). Contours run from  $3.125 \times 10^{-18} \text{ erg s}^{-1} \text{ cm}^{-2} \text{ arcsec}^{-2}$  to  $2 \times 10^{-16} \text{ erg s}^{-1} \text{ cm}^{-2} \text{ arcsec}^{-2}$  and are spaced by factors of 2. The 100 kpc [O II] nebula is  $\approx 10$  times the size of the galaxy. (c) F150LP image of Makani, drizzled to match the KCWI pixel scale ( $0''.2914 \times 0''.2914$ ). Contours are spaced 4 times apart from  $3.125 \times 10^{-17} \text{ erg s}^{-1} \text{ cm}^{-2} \text{ arcsec}^{-2}$  to  $8 \times 10^{-15} \text{ erg s}^{-1} \text{ cm}^{-2} \text{ arcsec}^{-2}$ . We estimate the surface brightness by multiplying the count rate by PHOTFLAM and PHOTBW and dividing by pixel area in  $\text{arcsec}^{-2}$ . (d) Matching F165LP image, with contours down to  $6.25 \times 10^{-17} \text{ erg s}^{-1} \text{ cm}^{-2} \text{ arcsec}^{-2}$ . Some extended emission is evident in the uniformly binned ACS-SBC images.

reproject (T. Robitaille et al. 2020) to the WFC3 image to resample to an integer multiple of the KCWI platescale:  $0''.036425 \text{ pixel}^{-1} = 0''.2914 \text{ pixel}^{-1}/8$ . This facilitates precisely coregistering the KCWI [O II] image. We then computed the coordinate of the centroid of the resulting WFC3 reprojection. The result is R.A. =  $319^{\circ}600'245'' = 21^{\text{h}}18^{\text{m}}24^{\text{s}}06$ ,  $\delta = 0^{\circ}29151'' = 0^{\circ}17'29''.44$ .

We thus obtained a WCS-aligned image and variance map in each filter with pixel scale  $0''.2914 \times 0''.2914$ . We show these images alongside the WFC3 and [O II] images in Figure 3, after dark subtraction (see below). We make an initial surface brightness estimate for each pixel by multiplying the count rate by the PHOTFLAM and PHOTBW values listed in the image headers and dividing by the area of each pixel in  $\text{arcsec}^{-2}$ . Some extended emission is already evident.

Since we eliminated exposures with high dark current and inversely weighted each image by the dark level before drizzling, we expected the combined image to have a spatially uniform dark pattern that fills the FOV. In practice, in each image we found a mild curvature in the dark current with a shallow peak near or underneath the expected signal from the galaxy. This gradient results from the overlapping dark current halo structures, as they fill a much larger area on the detector than the galaxy. To subtract the dark current, we then masked out the astrophysical structure in each image in an oval region. This structure was visible in each image prior to subtraction. As this structure is similar to that seen in the light of [O II], as discussed below, we used the [O II] image as a reference during the masking process because of its higher signal-to-noise ratio (S/N). We also masked those pixels whose values were more than  $2.5\sigma$  away from the median in each image. We then fit the unmasked data points in each image with a two-dimensional polynomial. Two-dimensional polynomials of degree 3 and 5 were used as background models for the F150LP image and F165LP images, respectively. We subtracted the model from each image to create a background-subtracted image for each filter with pixel scale  $0''.2914 \times 0''.2914$ . The F150LP background averages  $1 \times 10^{-4} \text{ counts s}^{-1} \text{ pixel}^{-1}$  over the region of detected astrophysical signal (see Section 3.1) so that the Poisson noise from the galaxy is greater than the dark current Poisson noise over the detection region. However, the F165LP dark current

is higher, ranging from  $5 \times 10^{-4} \text{ counts s}^{-1} \text{ pixel}^{-1}$  in the center down to  $2 \times 10^{-4} \text{ counts s}^{-1} \text{ pixel}^{-1}$  at the edge of the observed signal (see below in Section 3.1 for further discussion). Thus the dark current dominates the noise budget for the F165LP data at radii  $r \gtrsim 2''.5$ .

As the observed signal is very faint we further binned these images to enhance their S/N. We applied Voronoi tessellation to the background-subtracted F150LP image with a target  $S/N \gtrsim 7$  (M. Cappellari & Y. Copin 2003). During the binning process we weighted each pixel by  $\omega_i = |S_i/N_i^2|$ , which maximizes S/N while eliminating the contribution of pixels with significant noise and no signal (J. G. Robertson 1986; M. Cappellari & Y. Copin 2003). Since O VI lies at the peak of the F150LP throughput curve (Figure 1), we used the resulting Voronoi bins from F150LP to bin other images to a common set of spatial bins. These include the F165LP images, a difference image, and the [O II] image.

In Figure 4 we show the Voronoi-binned F150LP, F165LP, and F150LP – F165LP images and the S/N per bin of each of these images. Prior to Voronoi binning, we also median filter each image with a 5 pixel box and overlay these contours in each panel of Figure 4 for comparison. As we discuss below, these Voronoi-binned and median-filtered images more fully reveal the extent of the UV emission.

### 3. Results

#### 3.1. Morphology and Extent

The F150LP and F165LP images (Figure 4) of Makani show a strongly peaked central source. At a spatial scale of  $0''.025 \times 0''.025$ , the UV emission resolves into a luminous core, a clumpy elongation to the east, and a diffuse halo. These structures extend to a radius of  $\approx 1''$  and are similar, although not identical, to those seen in the rest-frame optical. P. H. Sell et al. (2014) fit an  $n = 4$  Sérsic and point-source model to the HST F814W image (rest-frame  $V$  band) of Makani (Figure 3(a)). This leaves a 10% flux residual, primarily in two tidal tails to the east and southwest. We leave the details of the  $r < 1''$  UV emission to future work but include in this section a few salient points. When binned to match the KCWI pixel scale of  $0''.2914 \times 0''.2914$ , the eastern elongation is visible in the centermost pixels in both filters (Figures 3(c)–(d)).

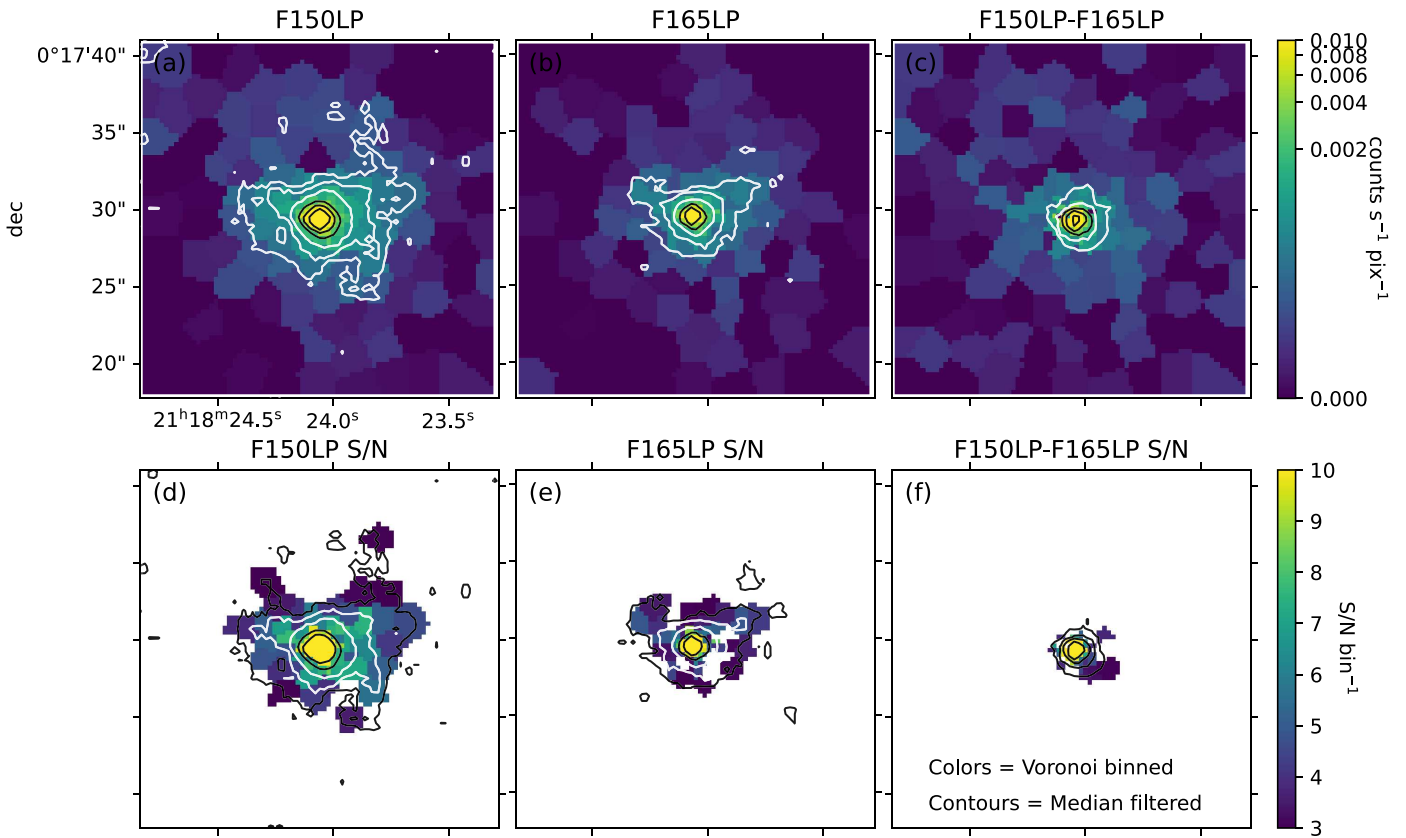


**Figure 4.** (a)–(c) Images of F150LP, F165LP, and the difference F150LP – F165LP, respectively. Colors show Voronoi-binned images, while contours display uniformly binned images, which are median filtered with a 5 pixel box. The color bar at the top right maps colors to counts  $\text{s}^{-1} \text{pixel}^{-1}$ , while contours range from  $1 \times 10^{-2}$  counts  $\text{s}^{-1} \text{pixel}^{-1}$  down to  $3.125 \times 10^{-4}$  or  $6.25 \times 10^{-4}$  and are separated by factors of 2. (d)–(e) Same as the top row, except S/N rather than intensity. Colors show S/N per Voronoi bin, as mapped by the color bar at the bottom right. Bins with S/N < 3 are not shown. Contours display S/N per pixel in the median-filtered images and associated error. They are separated by factors of 2, ranging from 10 down to 0.6125 or 1.25.

At radii of  $1''$  to  $5''$ , UV emission extends away from the center to the east and west, in the same directions as the highest surface brightness [O II] emission. The median-filtered and Voronoi-binned images reveal this emission most clearly (Figures 4(a)–(b)). We show a direct comparison in Figure 5. We also plot azimuthally averaged radial profiles of the drizzled images and their difference in Figure 6(a) and an S/N radial profile of each in panel (b).

The F165LP image has its highest surface brightness extensions  $\approx 5''$  to the northeast and northwest, with fainter emission to smaller radii in other directions (Figures 4(b) and (e)). These northeast and northwest extensions are at the bases of the two lobes of the northern half of the [O II] hourglass (Figures 5(b) and (d)). The radial S/N profile confirms that the F165LP emission is only detected above  $2\text{--}3\sigma$  at  $r < 5''$  (Figure 6(b)).

The F150LP emission is much more extended and bears a strong resemblance to the [O II] morphology. The Voronoi-binned data show  $3\sigma$  detections out to  $r = 8''$  (Figure 4(d)). The radial profile confirms azimuthally averaged emission at  $2\text{--}3\sigma$  out to  $r \approx 8''.5$  (Figure 6(b)). The radius of the [O II] nebula is also  $8''\text{--}9''$  (D. S. N. Rupke et al. 2019). The F150LP emission is present in all four lobes of the [O II] hourglass structure, as seen in both the Voronoi-binned and median-smoothed data (Figures 5(a) and (c)).

Considering also the data at lower significance (down to S/N  $\approx 2$ ), the F150LP data fully outline the cavity seen in the northern half of the [O II] hourglass (Figures 5(a) and (c)).

Although the southern half of the hourglass does not show a completely enclosed void in [O II], an emission minimum between two lobes is evident in the UV, as it is in [O II].

The difference image, F150LP – F165LP, shows significant emission only at  $r < 2''.5$  (Figure 6(b)). This emission is not symmetric but is slightly extended to the west (Figures 4(c) and (f)).

As we discuss above (Section 2.1), the emission in F150LP contains the light through the F165LP filter plus emission from 1450 to  $\approx 1600 \text{ \AA}$  (Figure 1). Additionally, the throughput of F150LP in the nonoverlap region is up to 4 times higher than in F165LP. As expected, the count rate per pixel  $C$  is thus higher in F150LP than in F165LP at all radii (Figure 6(a)).

The radial profiles of F150LP, F165LP, and F150LP – F165LP all show a similar decline with increasing radius (Figure 6(a)). The F165LP and F150LP – F165LP images decline to  $C = 1 \times 10^{-4}$  counts  $\text{s}^{-1} \text{pixel}^{-1}$  at  $\approx 5''$ . The F150LP profile declines to this count rate at  $\approx 7''$  to  $8''$ . The noise floor in these images at about this level arises largely due to Poisson noise from dark counts. In particular, the combined dark level subtracted from the F165LP image is  $\approx 3\times$  higher than that of the F150LP image over the  $0''$  to  $10''$  range. Thus, even though there are more astrophysical counts in the F150LP image, which in turn increases the Poisson noise, the noise is higher in our F165LP image due to increased dark current. The Poisson noise in the difference image is, of course, higher than in both.

As we discuss above, the radial significance cutoffs of each image are  $8''.5$  for F150LP,  $5''$  for F165LP, and  $2''.5$  for

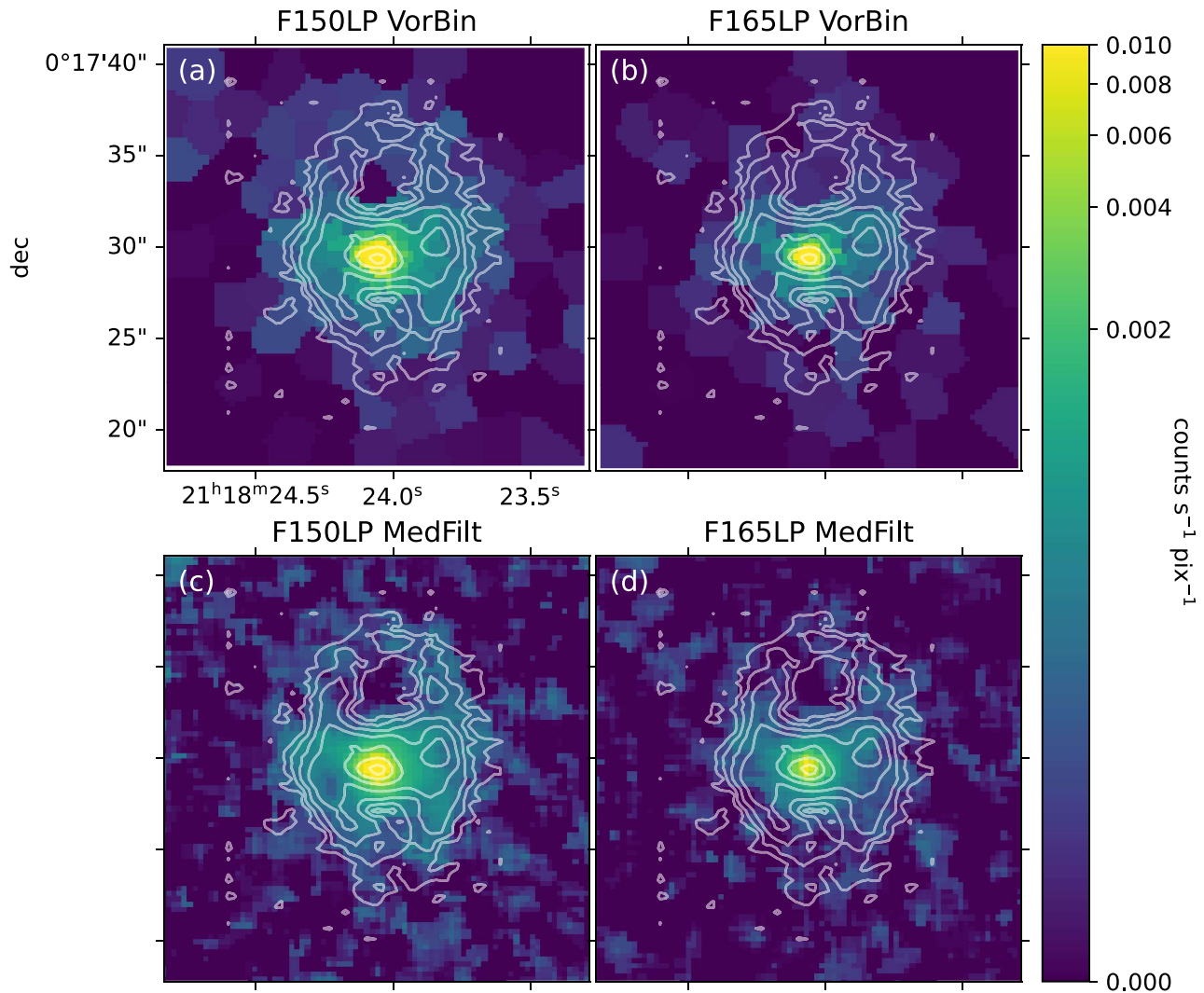


**Figure 5.** A comparison of [O II] and UV morphologies. (a) Voronoi-binned F150LP with [O II] contours overlaid. The Voronoi image is identical to Figure 4(a). Contours are the same as in Figure 3(a). (b) Voronoi-binned F165LP with [O II] contours. (c) [O II] on median-smoothed F150LP. (d) Smoothed F165LP, [O II] contours. These images show the close morphological correspondence between F150LP and [O II]. This correspondence is less prominent in F165LP, likely due to noise from higher dark current.

F150LP – F165LP. We attribute this in part to the decline in sensitivity across these images, but we also discuss astrophysical reasons for the difference below (Section 3.2).

A further source of potential error is uncertainty in the shape of the dark current pattern. In Figure 6(a), we show the gradient in the dark model for each image. For F165LP in particular, this gradient reaches  $-4 \times 10^{-5}$  counts  $s^{-1}$  pixel $^{-1}$  arcsec $^{-1}$  at  $r > 7''$ . The dark model is quite smooth, so this has no impact on discrete features such as those seen in Figure 4. However, all three radial profiles appear to continue to decline slightly beyond their significance cutoffs. This could be in part due to model errors in the dark profile at these radii. Alternatively, it may be due to the low-count Poisson statistics that dominate these regions with little or no astrophysical signal.

### 3.2. Origin of Emission

We expect the regions within the central  $\approx 1''$  to be dominated by UV continuum and/or Ly $\alpha$  emission, since this is where starlight and star formation in the system are concentrated. The compact starlight in Makani is evident from optical photometry.

Makani has a half-light radius of  $0''.4$  in the HST F814W WFC3 image (P. H. Sell et al. 2014), although this significantly overestimates the size of the compact core due to the tidal features to the east and southwest (Section 3.1). These tidal features extend to  $r = 2''$ —within which 98% of the rest-frame  $V$ -band light is contained, according to circular aperture photometry of the F814W image (Figure 3(a)). Photometry of deep, ground-based Dark Energy Spectroscopic Instrument (DESI) Legacy Imaging Survey DR10.1 data of Makani (D. Lang et al. 2016; A. Dey et al. 2019) does not find additional flux at larger radii. P. H. Sell et al. (2014) measure  $m_{814}^{AB} = 18.54$  from HST, which is only 7% different from  $m_{814}^{AB} = 18.61$  inferred from the ground-based Legacy data.<sup>15</sup> Radio emission tracing  $>200 M_{\odot} \text{ yr}^{-1}$  star formation is unresolved with  $2''$  resolution imaging (G. C. Petter et al. 2020). Line emission tracing stellar photoionization is confined primarily to the inner  $\sim 1''$  (D. S. N. Rupke et al. 2023).

<sup>15</sup> To estimate the Legacy flux in the HST passband, we fit a spectral energy distribution model to the Legacy Survey data and process it through `stsynphot`. These fluxes are not corrected for Galactic extinction.

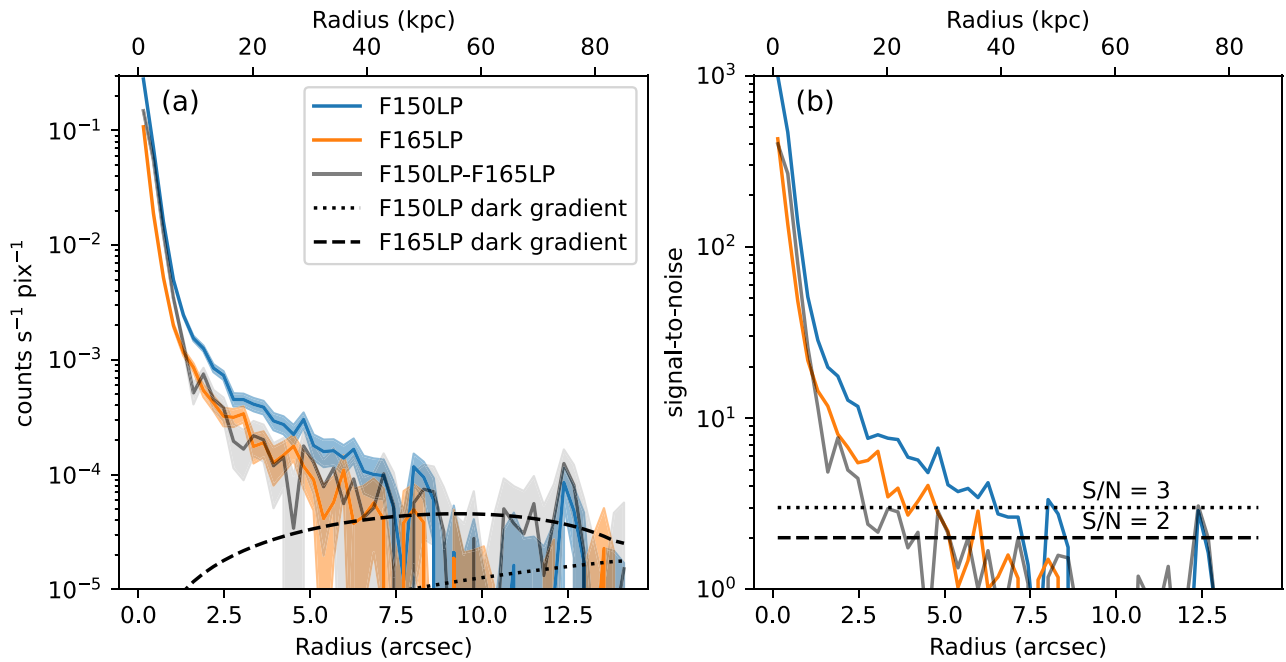


**Figure 6.** (a) Radial profiles of F150LP and F165LP images from Figure 3, as well as that of a difference image. The  $1\sigma$  errors are shown as shaded regions. The F150LP and F165LP profiles are similar in shape, but there is more flux in the F150LP image at all radii. The difference profile is most similar to the F165LP profile. The dashed and dotted lines are the radial gradients in the dark model and illustrate their potential contribution to the systemic uncertainty. The units of these gradients are  $\text{counts s}^{-1} \text{pixel}^{-1} \text{arcsec}^{-1}$ . (b) S/N of radial profiles. Dashed and dotted lines denote S/N = 2 and 3 thresholds. These illustrate that the F165LP image only shows a significant detection at radii  $r \lesssim 5''$  and that the difference image is even less informative.

At intermediate radii of  $1''$ – $2''$ , the UV emission seen in the SBC data is negligibly contaminated by the wings of the nuclear point-spread function (PSF). By finely sampling the F150LP PSF, M. Hayes et al. (2016) find that the surface brightness of a point source declines to  $\approx 5 \times 10^{-5}$  times the peak at  $r = 2''$ . At a coarser radial binning of  $0''.1$ —more like the binned Makani data—this contrast decreases to  $\approx 1 \times 10^{-4}$  (R. J. Avila & M. Chiaberge 2016). In Makani, the surface brightness at the same radius from the peak is  $\approx 5 \times 10^{-3}$  to  $1 \times 10^{-2}$  times the peak brightness (Figure 6(a))—that is, at least 50 times the expected contribution from the PSF.

Nebular continuum from excited and/or ionized hydrogen is another possible emission channel in the UV optical. H II regions produce free-bound and free-free emission that dominates across most of the optical (R. L. Brown & W. G. Mathews 1970), while the 2-photon ( $2\gamma$ ) emissivity from  $2s \rightarrow 1s$  peaks at  $1420 \text{ \AA}$  in wavelength space (H. Nussbaumer & W. Schmutz 1984). At the wavelengths of concern, only the  $2\gamma$  emission could contribute, and only at wavelengths  $>1216 \text{ \AA}$ . M. Dijkstra (2009) show that this emission can, in fact, arise in cooling gas (see Section 4.3). However, the predicted equivalent width of  $\text{Ly}\alpha$  in such cooling gas, when compared to the nebular continuum, is  $>1000 \text{ \AA}$  (M. Dijkstra 2009). Given that only  $\approx 150 \text{ \AA}$  of continuum lies within the filter above  $\text{Ly}\alpha$  (Figure 1), this contribution might account for  $\sim 15\%$  of any photons attributed to  $\text{Ly}\alpha$ . We ignore this contribution when calculating any  $\text{Ly}\alpha$  properties. Regardless, the procedure below removes this contribution from the F150LP light along with  $\text{Ly}\alpha$ .

Reflection of  $1350$ – $2800 \text{ \AA}$  continuum and optical-line emission from dust in the inner halos of galaxies and in galactic winds is observed in nearby star-forming galaxies (S. M. Scarrott et al. 1991; C. G. Hoopes et al. 2005; E. Hodges-Kluck et al. 2016). This process could contribute to the F150LP and F165LP bands at radii out to  $15$ – $20 \text{ kpc}$  ( $3''$ ),

as the scattering albedo is high down to these rest wavelengths (B. T. Draine 2003). Dust extinction and continuum emission are observed out to these radii in Makani, as are neutral atomic and molecular phases that trace dusty gas (D. S. N. Rupke et al. 2019, 2023; S. Veilleux et al. 2025). We cannot at present directly constrain the magnitude of possible UV scattered light, although the UV emission does not obviously correlate morphologically with the dust emission (S. Veilleux et al. 2025). In the analysis below we assume this contribution is negligible but return to the possibility when it is salient.

Thus, at radii  $r \gtrsim 1''.5$ , the emission is dominated by line emission rather than continuum emission, aside from a possible contribution from starlight scattered by dust at  $1''.5 < r < 3''$ . Together with O VI and  $\text{Ly}\alpha$ , M. Hayes et al. (2016) consider other emission lines that potentially arise in the narrow bandpasses of these filters:  $\text{Ly}\beta$ , scattered C II  $1036 \text{ \AA}$ , and fluorescent C II\*  $1036 \text{ \AA}$ . Based on the lack of observed  $\text{Ly}\beta$  or C II in local starbursts (J. P. Grimes et al. 2009; T. M. Heckman et al. 2011; A. Henry et al. 2015; M. Hayes et al. 2016), the contribution of these lines is likely negligible.  $\text{Ly}\alpha$  halos in these systems arise due to many resonant scatterings, while  $\text{Ly}\beta$  is subject to reemission as  $\text{H}\alpha$  photons. Even if  $\text{Ly}\beta$  arose from direct emission in shocks, it is likely much fainter than  $\text{Ly}\alpha$  (A. Lehmann et al. 2020). A high-ionization line that often accompanies O VI in quasar spectra is N V  $1238, 1243 \text{ \AA}$  (e.g., S. Veilleux et al. 2022); this could appear in the red tail of the F165LP filter. However, it is expected to be weak compared to O VI in shocked gas (M. G. Allen et al. 2008) and is much less luminous than  $\text{Ly}\alpha$  even in active galactic nuclei (AGNs). These considerations imply that the extended emission in F150LP is due solely to O VI and  $\text{Ly}\alpha$ , while in F165LP it is due only to  $\text{Ly}\alpha$ .

The presence of both O VI and  $\text{Ly}\alpha$  in F150LP is indicated by the higher count rate and larger observed extent in F150LP

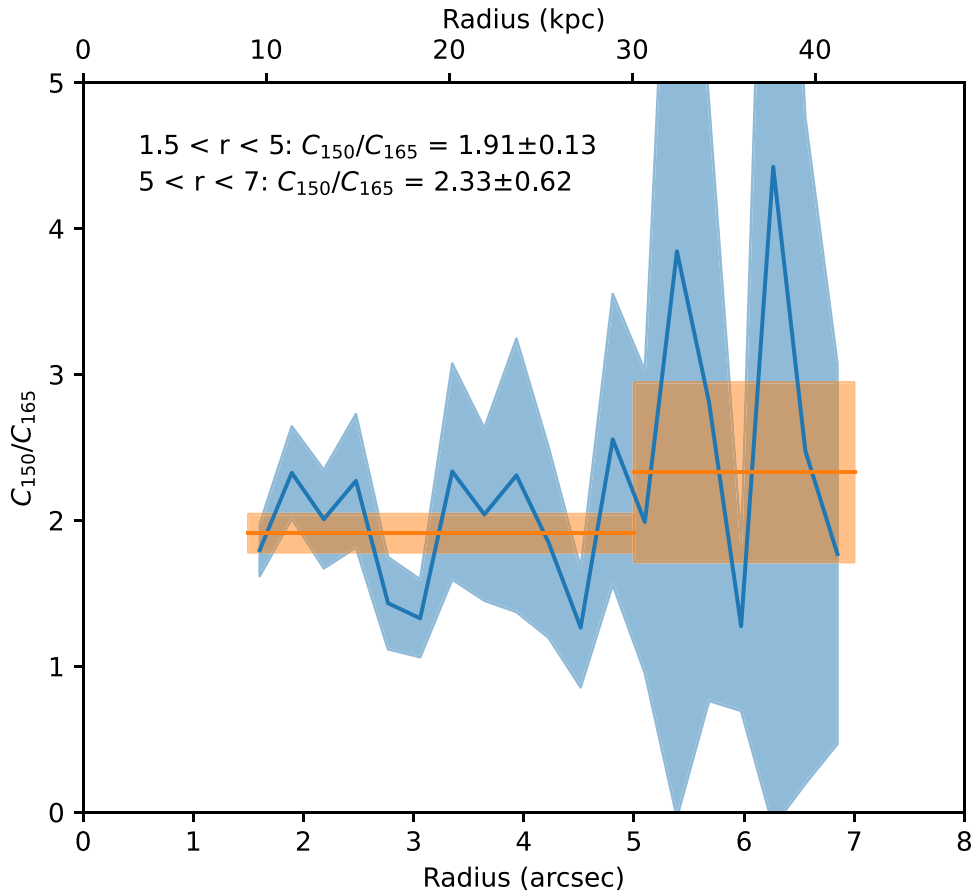


**Figure 7.** The ratio  $\mathcal{R} \equiv C_{150}/C_{165}$  vs. radius outside the continuum-dominated regions and out to the nebula edge. The blue line and shaded region indicate a radial profile and  $1\sigma$  error. The orange lines and shaded regions indicate the mean and standard deviation in the two circular annuli shown in the legend.

compared to F165LP (Section 3.1). To quantify the relative contribution, we use the count rate ratio  $\mathcal{R} \equiv C_{150}/C_{165}$ . Due to the low S/N in the F165LP image (Figure 4(e)), particularly at  $r > 5''$  (Figure 6(b)), it is difficult to compute  $\mathcal{R}$  across the nebula, even by Voronoi bin or radial profile. Instead, we compute two values, one each for the inner and outer regions of the nebula. In Figure 7 we show that  $\mathcal{R}$  is fairly constant over the inner  $1''.5 < r < 5''$  region in which F165LP shows significant emission, with  $\mathcal{R}_{\text{inner}} = 1.91 \pm 0.13$ . In the outer,  $5'' < r < 7''$  region, the ratio is much less constrained:  $\mathcal{R}_{\text{outer}} = 2.33 \pm 0.62$ . This is consistent with a constant value of  $\mathcal{R}$  but also with an increasing value with increasing radius. In other words, 44%–51% of counts in the F150LP image arise from O VI at  $1''.5 < r < 5''$ . At larger radius, the possible range is 42%–66%.

The lack of extended emission in the difference image F150LP – F165LP (Figures 4(c) and (f)) appears to contradict this. That is, at face value it implies there is no O VI emission in the extended nebula. Subtracting F165LP—which contains only Ly $\alpha$ —removes any significant signal. However, as we discuss in Section 3.1, this is driven by Poisson noise from dark current in the F165LP image. To demonstrate this we create a model of the F150LP image from the F150LP data. We scale F150LP by the measured values of  $\mathcal{R}_{\text{inner}}$  and  $\mathcal{R}_{\text{outer}}$  over the corresponding radii to mimic the F165LP signal but keep the measured noise values from the F165LP data. The resulting model signal strongly resembles the observed F165LP image and radial profile of both signal and S/N (Figure 8). We thus conclude that the small apparent size of F165LP, and even smaller size of the difference image, is due to the increased noise and decreased

signal when the images are subtracted, rather than a deficit of O VI emission in the F150LP image.

### 3.3. Line Fluxes and Line Ratios

To convert count rates to astrophysical fluxes, we use the throughput  $\mathcal{T}$  in F150LP and F165LP at the wavelengths of redshifted O VI and Ly $\alpha$ . In the emission-line-only region, the count rates in each filter are given by

$$C_{150} = \mathcal{C}(F_{\text{O VI}} \mathcal{T}_{\text{O VI}}^{150} + F_{\text{Ly}\alpha} \mathcal{T}_{\text{Ly}\alpha}^{150}) \quad (1)$$

and

$$C_{165} = \mathcal{C}(F_{\text{Ly}\alpha} \mathcal{T}_{\text{Ly}\alpha}^{165}), \quad (2)$$

where  $\mathcal{C}_j$  is the conversion from flux to counts in filter  $j$ ,  $F_i$  are the intrinsic fluxes of each line  $i$ , and  $\mathcal{T}_i^j$  are the throughput values at the wavelength of the given line  $i$  and filter  $j$ . Here we assume the wavelength dependence of the ACS-SBC response is captured completely in  $\mathcal{T}$  and  $\mathcal{C}$  is thus a constant.

Combining Equations (1) and (2), we express the O VI flux as

$$F_{\text{O VI}} = \frac{C_{150}}{\mathcal{C}\mathcal{T}_{\text{O VI}}^{150}} \left( 1 - \frac{\mathcal{T}_{\text{Ly}\alpha}^{150}}{\mathcal{T}_{\text{Ly}\alpha}^{165}} \mathcal{R}^{-1} \right). \quad (3)$$

(As a reminder, we defined  $\mathcal{R} = C_{150}/C_{165}$  in Section 3.2.) We assume that the F150LP image—outside of  $r \gtrsim 1''.5$ —describes the morphology of both O VI and Ly $\alpha$ . We estimate the quantity

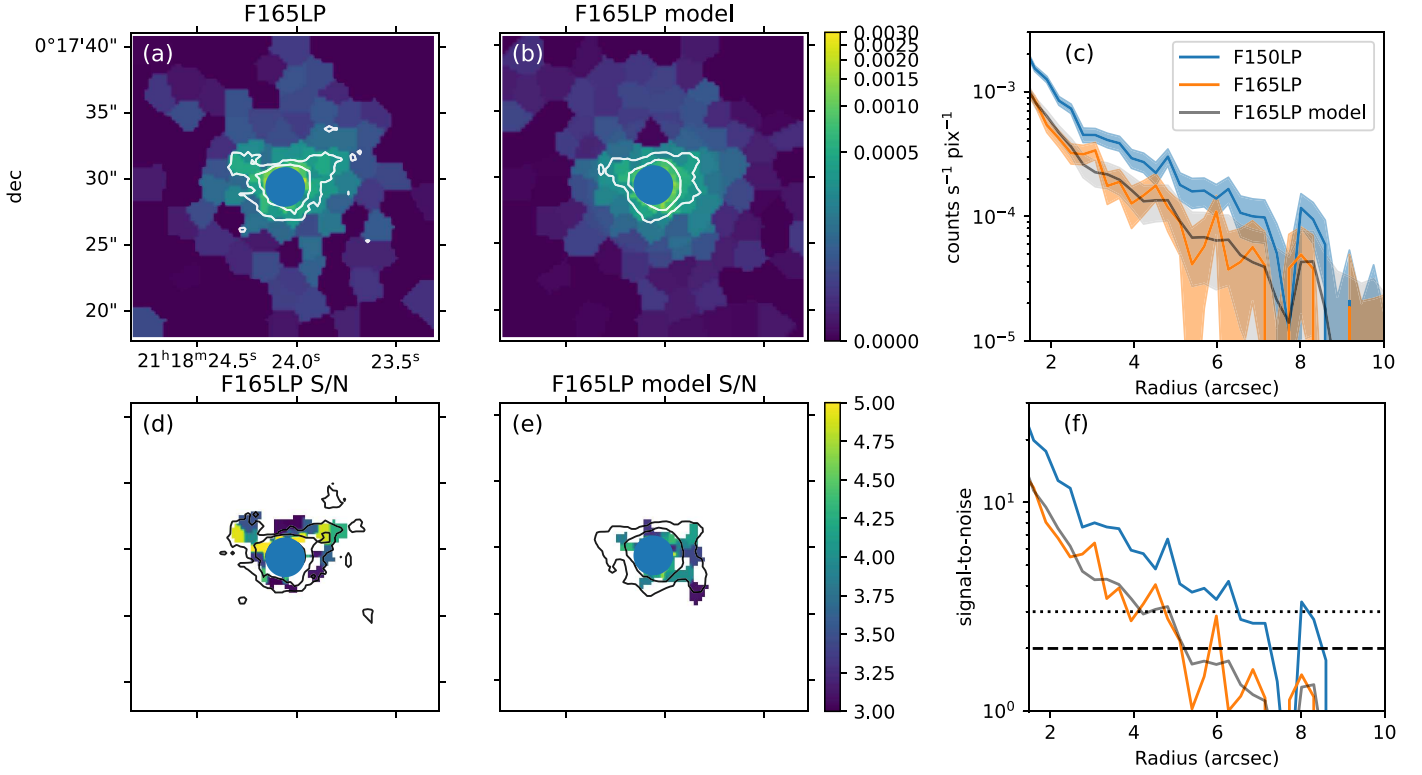


**Figure 8.** Observed F165LP images and radial profiles, compared to those from a model using scaled F150LP data. (a) The Voronoi-binned and median-smoothed F165LP images of Makani, as in Figure 4(b). We mask  $r < 1''.5$ , which is dominated by continuum emission, and reduce the range of the color map to emphasize lower fluxes. The contours are the same as in Figure 4(b). (b) A model F165LP image, created by scaling the F150LP image assuming  $C_{165} = \mathcal{R}_{\text{inner}} C_{150}$  over  $1''.5 < r < 5''$  and  $C_{165} = \mathcal{R}_{\text{outer}} C_{150}$  at  $r > 5''$ . Note the similarity to panel (a). (c) Radial profiles of the observed F150LP and F165LP images and the model F165LP image, zooming in on radii expected to be emission line dominated. The model and observed F165LP profiles are similar, by construction. (d) Same as Figure 4(d), but modified as described for panel (a). Only bins with S/N > 3 are shown. (e) A model F165LP S/N map, where the signal is from the model F165LP image, while the noise is equal to the observed F165LP values. Note the similar morphology to panel (d), illustrating that the apparent compactness of the F165LP image may be driven by the larger noise compared to F150LP, coupled with a lower signal. (f) Radial S/N profiles. Again, this illustrates that the apparent differences in morphology between F150LP and F165LP may be due to increased noise.

$\mathcal{C}_{\text{O VI}}^{150} \equiv \mathcal{C}_{\text{O VI}}^{\mathcal{T}^{150}}$  using a synthetic emission-line profile input to `synphot` and `stsynphot` (STScI Development Team 2018, 2020), while  $\mathcal{T}_{\text{Ly}\alpha}^{150}$  and  $\mathcal{T}_{\text{Ly}\alpha}^{165}$  come directly from the response function (Section 2.1, Figure 1). The result is

$$F_{\text{O VI}} = (7.68 \times 10^{-15} \text{ erg s}^{-1} \text{ cm}^{-2}) C_{150} (1 - 1.07\mathcal{R}^{-1}), \quad (4)$$

where  $C_{150}$  is in  $\text{counts s}^{-1}$ .

To compute  $F_{\text{Ly}\alpha}$ , we can invert Equation (2) and input  $C_{165}$ . As before, we use `synphot` and `stsynphot` to estimate  $\mathcal{C}_{\text{Ly}\alpha}^{165} \equiv \mathcal{C}_{\text{Ly}\alpha}^{\mathcal{T}^{165}}$ . Alternatively, we can use the definition of  $\mathcal{R}$  and rearrange Equation (2) to express the Ly $\alpha$  flux in terms of  $C_{150}$ :

$$F_{\text{Ly}\alpha} = \frac{C_{150}}{\mathcal{C}_{\text{Ly}\alpha}^{165}} \mathcal{R}^{-1} = (3.20 \times 10^{-14} \text{ erg s}^{-1} \text{ cm}^{-2}) C_{150} \mathcal{R}^{-1}. \quad (5)$$

These yield similar results. For a more conservative approach, we adopt the simple inverse of Equation (2). We apply Equation (4) to the radial profile of  $C_{150}$  and Equation (5) to the radial profile of  $C_{165}$  (Figure 6(a)) over  $1''.5 < r < 9''$ . This ignores the inner region contaminated by continuum but extends outward to the  $2\sigma$  detection region of the  $C_{150}$  map (Figure 6(b)). We use the measured values of  $\mathcal{R}_{\text{inner}}$  and  $\mathcal{R}_{\text{outer}}$ , with the latter applying at all radii  $r > 5''$ . We also correct for Milky Way extinction using

reddening maps derived from DESI Survey observations of stellar spectra. We take the average of the  $(g-r)$  and  $(r-z)$  maps,  $E(B-V) = 0.0587$  (R. Zhou et al. 2024). We apply the Milky Way extinction model with  $R_V = 3.1$  from K. D. Gordon et al. (2023) using the `dust_extinction` package (K. D. Gordon 2024). The resulting radial profiles are similar in shape to that of [O II] (Figure 9). We apply the same procedure to produce flux maps of O VI emission (Figure 10).

With our flux-calibrated O VI image, we can compute the observed (attenuated) line ratio [O II]/O VI in each Voronoi bin, which we show in Figure 11. The resulting values are in the range 0.05–1.3. They appear to be elevated to the east and west of the nucleus along the rims of the hourglass shape and lower directly north and south. We also plot these values against the [O II] surface brightness  $\Sigma([\text{O II}])$  and projected radius. It is apparent that higher [O II]/O VI values correspond to regions of higher [O II] surface brightness and decline at both small and large radius.

Combining Equations (1) and (2), we can also write the flux ratio of the two lines in the extended nebula as

$$\frac{F_{\text{O VI}}}{F_{\text{Ly}\alpha}} = \frac{\mathcal{T}_{\text{Ly}\alpha}^{150}}{\mathcal{T}_{\text{O VI}}^{150}} \left( \mathcal{R} \frac{\mathcal{T}_{\text{Ly}\alpha}^{165}}{\mathcal{T}_{\text{Ly}\alpha}^{150}} - 1 \right) = 0.20(0.93\mathcal{R} - 1). \quad (6)$$

Using our measured values for  $\mathcal{R}$ , and correcting for Milky Way extinction as above, we thus find  $(F_{\text{O VI}}/F_{\text{Ly}\alpha})_{\text{inner}} = 0.16 \pm 0.03$  and  $(F_{\text{O VI}}/F_{\text{Ly}\alpha})_{\text{outer}} = 0.24 \pm 0.12$ .

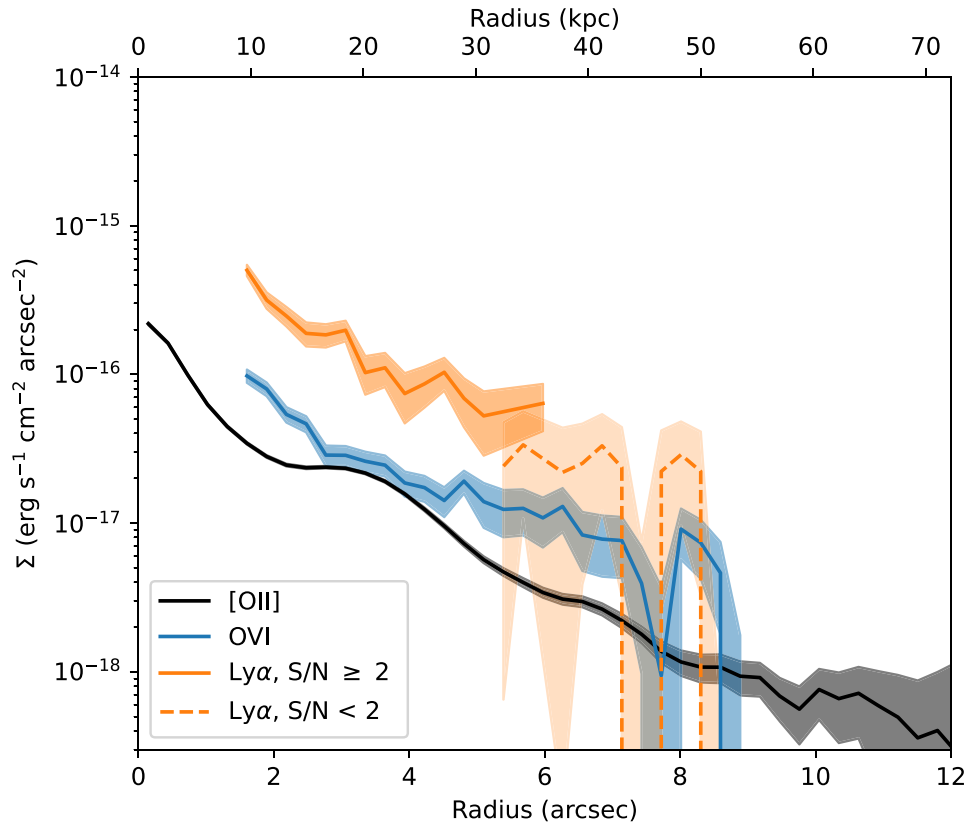


**Figure 9.** Radial surface brightness profiles of O VI and Ly $\alpha$ , with [O II] (D. S. N. Rupke et al. 2019) shown for comparison. We show only radial bins dominated by line emission. We have converted counts to line fluxes in F150LP and F165LP using Equations (4) and (5) and flux to surface brightness using the drizzled pixel scale (Section 2.2). We plot the high-significance and low-significance Ly $\alpha$  bins separately. Shaded regions represent  $1\sigma$  errors, including uncertainties in both count rates ( $C_{150}$  and  $C_{165}$ ) and average  $\mathcal{R}$  (Figure 7).

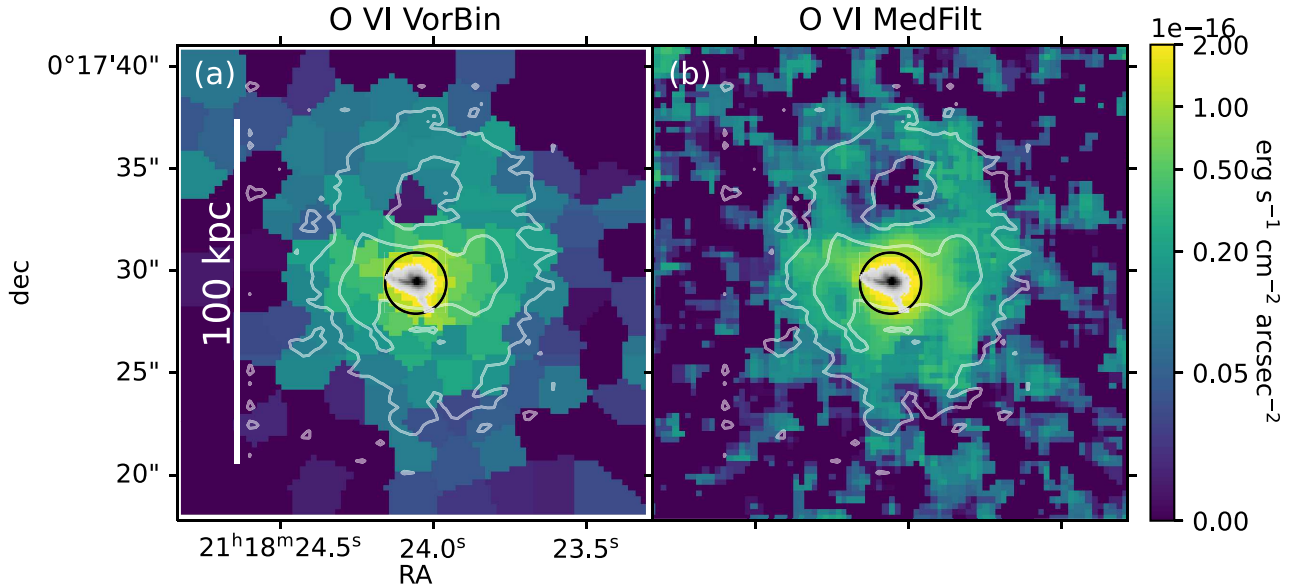


**Figure 10.** Voronoi-binned and median-filtered flux maps of O VI, as computed from Equation (4). We use the measured values of  $\mathcal{R}_{\text{inner}}$  and  $\mathcal{R}_{\text{outer}}$ , shown in Figure 7, to correct for Ly $\alpha$  contamination. We delineate the inner, continuum-dominated region with a  $1/5$  circle and overlay the F814W starlight image.

## 4. Discussion

We have shown that the Makani wind nebula, previously imaged in the low ionization emission lines of [O II] (D. S. N. Rupke et al. 2019), also shows high ionization O VI and Ly $\alpha$  emission that is spatially coincident with [O II] throughout the observed volume.

### 4.1. Integrated Wind Properties

As we discuss in Section 1, the single, spatially resolved image of an O VI halo is J1156 (M. Hayes et al. 2016). This  $z = 0.235$  galaxy is a low-mass ( $10^9 M_{\odot}$ ) galaxy with  $\text{SFR} \approx 30 M_{\odot} \text{ yr}^{-1}$ . The radial surface brightness profile of this galaxy is consistent with an exponential profile with central

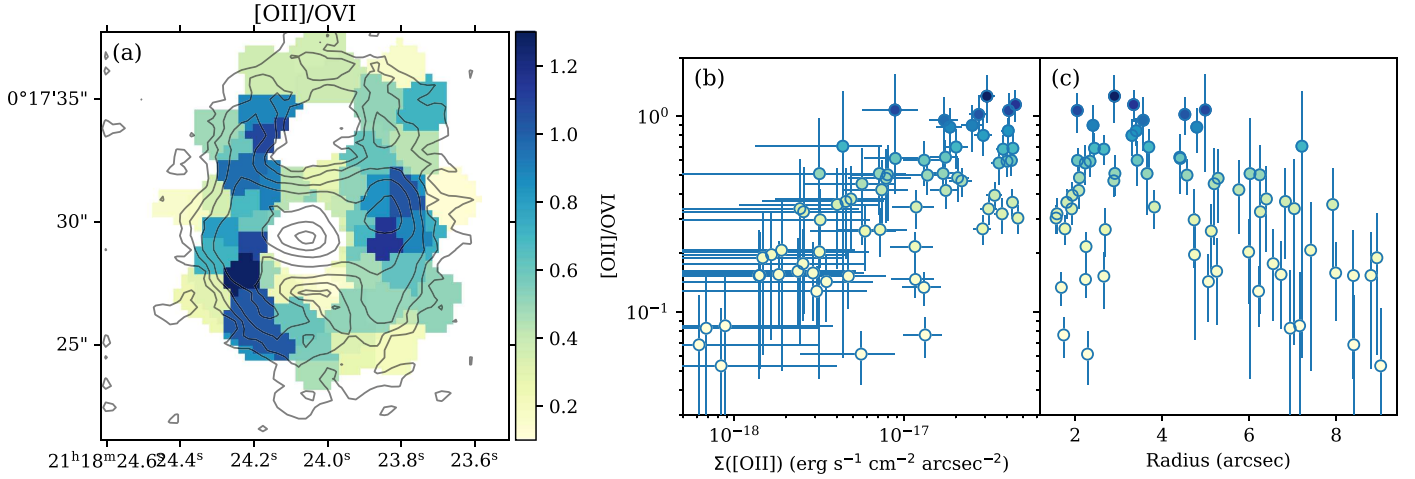


**Figure 11.** (a) Map of flux ratio  $F([O II] 3727, 3729 \text{ \AA})/F(O VI 1032, 1038 \text{ \AA})$ , with  $[O II]$  contours overlaid. We mask the  $r < 1''.5$  region and show only bins with  $S/N > 1$  in both lines. The ratio appears highest east and west, while it is lower directly north and south. (b)–(c): Line ratio vs.  $[O II]$  surface brightness and radius in each Voronoi bin. The errors shown are  $1\sigma$ , and the bins are colored by their line ratio as in panel (a).  $[O II] 3727, 3729 \text{ \AA}/O VI$  increases with increasing  $\Sigma([O II])$ . It peaks at radii  $2''\text{--}5''$ , primarily along the east and west sides of the hourglass shape, and declines at lower and higher radii.

surface brightness  $\Sigma_0 = 5.3 \times 10^{-17} \text{ erg s}^{-1} \text{ cm}^{-2} \text{ arcsec}^{-2}$  and exponential radius  $r_{\text{exp}} = 7.5 \text{ kpc}$ . This is equivalent to an  $n = 1$  Sérsic with effective (half-light) radius  $r_e = 1.6783 r_{\text{exp}} = 12.6 \text{ kpc}$ , with an extrapolated surface brightness at this radius of  $\Sigma_e = 2.0 \times 10^{-17} \text{ erg s}^{-1} \text{ cm}^{-2} \text{ arcsec}^{-2}$ . The scale of the O VI halo is about 10 times the scale of the photoionized H $\alpha$ - and Ly $\alpha$ -emitting gas in this system (M. Hayes et al. 2016). M. Hayes et al. (2016) infer a density of  $n_e \approx 0.5 \text{ cm}^{-3}$  for the coronal gas, and its kinematics imply an outflow.

In Figure 12 we compare J1156 to the radial surface brightness profile of Makani. As a reference point, we estimate the central surface brightness  $\Sigma_0(O VI)$  by scaling  $\Sigma_0([O II])$  using  $[O II]/O VI = 0.66 \pm 0.29$ . This is the mean and standard deviation measured in the Voronoi bins with  $\Sigma([O II]) > 2 \times 10^{-17} \text{ erg s}^{-1} \text{ cm}^{-2} \text{ arcsec}^{-2}$  (Figure 11(b)). We multiply the J1156 surface brightness by 0.51, which is the relative  $(1+z)^4$  dimming of itself and Makani, as if J1156 were observed to be at  $z = 0.459$  rather than 0.235. In this figure, we compare also to the surface brightness of the O VI detection in NGC 4631, which is of order  $1 \times 10^{-18} \text{ erg s}^{-1} \text{ cm}^{-2} \text{ arcsec}^{-2}$  at 4 kpc radius, if it were observed at the redshift of Makani (B. Otte et al. 2003).

The profile of O VI emission in Makani is well-fit by a double exponential profile. We use the `emcee` (D. Foreman-Mackey et al. 2013) minimizer in `lmfit` (M. Newville et al. 2024) to find the best-fit double exponential:

$$\Sigma(r) = \Sigma_0^{\text{in}} e^{-r/r_{\text{exp}}^{\text{in}}} + \Sigma_0^{\text{out}} e^{-r/r_{\text{exp}}^{\text{out}}}. \quad (7)$$

We set the upper bound of  $r_{\text{exp}}^{\text{in}}$  equal to the lower bound of  $r_{\text{exp}}^{\text{out}}$ . We also fix the amplitude  $\Sigma_0^{\text{in}}$  of the inner profile to equal 90% of the total amplitude  $\Sigma_0$ , as estimated from  $[O II]$ . In Table 1 we list the best-fit parameters.

To compute the integrated properties of the nebula, we take several approaches. First, we integrate the flux of the nebula over the observed Voronoi bins with  $r > 1''.5$  and  $S/N > 2$  detections. Second, we extrapolate the double exponential profile to 60 kpc and to  $\infty$ , for comparison. The first method does not include the unmeasured nuclear flux and yields about two-thirds of the flux of the profile integration method.

Integrating to  $\infty$  rather than 60 kpc increases the flux by about 10%; 22% of the total flux resides under the inner exponential. We find an effective (half-light) radius of 19–21 kpc, similar to that of  $[O II]$ , for which  $r_{\text{eff}} \approx 18 \text{ kpc}$  (D. S. N. Rupke et al. 2019). We also list these values in Table 1.

The Makani nebula is produced by multiple outflow episodes over several hundred Myr. It may thus be that the inner exponential corresponds to the recent episode II emission, while the outer exponential represents the more evolved episode I nebula. The entire O VI nebula is 20 times more luminous than that of J1156. This higher luminosity is consistent with the increase of CGM O VI absorbers with SFR (K. Tchernyshyov et al. 2023). Makani’s SFR is  $224\text{--}300 M_{\odot} \text{ yr}^{-1}$  (G. C. Petter et al. 2020), versus  $30 M_{\odot} \text{ yr}^{-1}$  in J1156. Similarly, the O VI surface brightness of NGC 4631—with SFR of  $3 M_{\odot} \text{ yr}^{-1}$  (M. Meléndez et al. 2015)—is of order 10 times smaller even than J1156 at comparable radii. These scalings are broadly consistent with the roughly linear relationship of  $L_{O VI}$  and SFR surface density in the simulations of M. Li et al. (2017a). Alternatively, some of the inner exponential in Makani could arise from starlight scattered off dust grains (Section 3.2). This would amount to at most 20% of the total O VI flux if the entirety of the inner exponential was due to this process.

The Ly $\alpha$  nebula in Makani is also bright and large. We apply Equation (5) to the  $C_{165}$  map and correct for Milky Way extinction. As with O VI, we then integrate over Voronoi bins with  $r > 1''.5$  and  $S/N > 2$  detections. The resulting flux and luminosity are  $(8.7 \pm 0.5) \times 10^{-15} \text{ erg s}^{-1} \text{ cm}^{-2}$  and  $(7.3 \pm 0.4) \times 10^{42} \text{ erg s}^{-1}$ . If the half-light radius of Ly $\alpha$  is similar to that of O VI, this places the Makani nebula in the Ly $\alpha$  blob class (M. Ouchi et al. 2020). In this context, it is consistent with other Ly $\alpha$  blobs that arise around massive, star-forming galaxies and AGN.

#### 4.2. In Situ Emission versus Scattered Light

O VI in the CGM has to date been observed primarily in absorption against background sight lines. Like other transitions that lead to absorption in diffuse interstellar gas, the lower level of the O VI 1032, 1038  $\text{\AA}$  transitions is the ground state (D. C. Morton 1991). O VI emission is produced by in situ

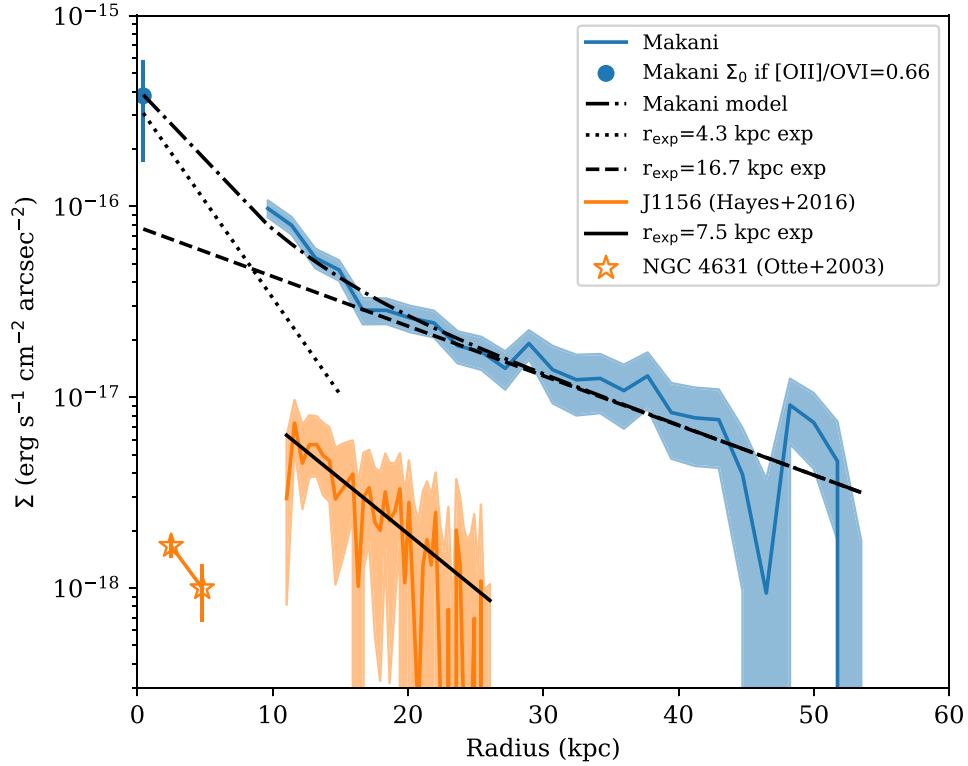


**Figure 12.** Surface brightness profile of O VI emission in Makani, J1156 (M. Hayes et al. 2016), and NGC 4631 (B. Otte et al. 2003) as a function of projected radius. The nuclear point of Makani is derived from [O II]. A double exponential model (Equation (7)) is overplotted. The J1156 and NGC 4631 data have been scaled downward by factors of  $\approx 2$  and  $\approx 5$ , as if they were observed at the redshift of Makani. The best-fit exponential model from M. Hayes et al. (2016) is also shown. The Makani nebula is significantly brighter and larger than that of J1156—with 20 times the total estimated luminosity—consistent with its 10 times higher SFR. The two-component fit may reflect the two outflow episodes. The inner exponential, containing 20% of the O VI light, may also have some contribution from dust scattering of starlight (Section 3.2).

**Table 1**  
O VI Measurements

Quantity	Value
Best-fit 2-exponential model parameters	
$\Sigma_0^{\text{in}}$	$3.42 \times 10^{-16} \text{ erg s}^{-1} \text{ cm}^{-2} \text{ arcsec}^{-2}$ [fixed]
$r_{\text{exp}}^{\text{in}}$	$(4.29 \pm 0.34) \text{ kpc}$
$\Sigma_0^{\text{out}}$	$(0.78 \pm 0.10) \times 10^{-16} \text{ erg s}^{-1} \text{ cm}^{-2} \text{ arcsec}^{-2}$
$r_{\text{exp}}^{\text{out}}$	$(16.68 \pm 1.01) \text{ kpc}$
Voronoi binned data, $S/N > 2$ , $r > 1''5$	
Flux	$(2.89 \pm 0.10) \times 10^{-15} \text{ erg s}^{-1} \text{ cm}^{-2}$
Luminosity	$(2.42 \pm 0.09) \times 10^{42} \text{ erg s}^{-1}$
2-exponential model, extrapolated to $\infty$	
Flux	$4.86 \times 10^{-15} \text{ erg s}^{-1} \text{ cm}^{-2}$
Luminosity	$4.06 \times 10^{42} \text{ erg s}^{-1}$
$r_{\text{eff}}$	21.42 kpc
2-exponential model, extrapolated to 60 kpc	
Flux	$4.39 \times 10^{-15} \text{ erg s}^{-1} \text{ cm}^{-2}$
Luminosity	$3.67 \times 10^{42} \text{ erg s}^{-1}$
$r_{\text{eff}}$	18.85 kpc

processes that excite the  $\text{O}^{+5}$  ions, like collisional heating or irradiation by local sources. However, as a so-called resonant line, it is also a channel for continuum scattering into the line of sight. Sighting “down the barrel” toward the starlight from a galaxy, an outflowing shell absorbs continuum at blueshifted

wavelengths and scatters photons back to the observer at redshifted wavelengths. This is the classic P-Cygni profile. More complicated gas and dust distributions result in other line shapes for resonant lines in a galactic wind, which are mainly variations on this theme (J. X. Prochaska et al. 2011).

A spherically symmetric, expanding nebula with no dust is the simplest galactic wind. When the emerging light is spatially and spectrally integrated over the continuum background source and larger-scale wind, the total equivalent width of a resonant line is zero (A. Verhamme et al. 2006; J. X. Prochaska et al. 2011). That is, the emission and absorption equivalent widths from scattering are equal in magnitude. Using this simple model, M. Hayes et al. (2016) estimated at least 6 times more O VI emission in J1156 overall than that observed only along the line-of-sight aperture to the starlight. In the starlight-only aperture covering J1156, the emission and absorption equivalent widths are approximately equal. Thus, the scattered light in this approximation accounts for at most one-sixth of the observed O VI emission in J1156. In Haro 11, another starburst with similar SFR to J1156, the integrated absorption and emission equivalent widths are approximately equal (J. P. Grimes et al. 2007).

We have no O VI spectroscopy of Makani from which to construct a similar argument. However, we can assume the spherically symmetric model and consider the possible magnitudes of line emission and absorption along the line of sight to the galaxy starlight. If the extended O VI emission we measure is stronger than the possible back-scattered emission along the same line of sight as any possible absorption—that

is, along the line of sight to the galaxy’s stars—than we can consider the emission to be dominated by in situ emission.

The starlight footprint of Makani is highly concentrated, with an aperture of radius  $1''$  containing 80%–90% of the UV-optical continuum (Sections 3.1–3.2). Such an aperture contains 13% of the O VI flux, as estimated from the 2-exponential model. To calculate the equivalent width of this emission, we assume the F150LP image is continuum dominated at  $r < 1''$  and use PHOTFLAM to estimate the total flux density  $F_{1605}$  at the filter pivot wavelength. The resulting rest-frame equivalent width of emission is  $7 \text{ \AA}$ .

For comparison, J. P. Grimes et al. (2009) report 1032 Å absorption-line equivalent widths of 0.2–1.7 Å in a sample of nearby starbursts. The total O VI 1032, 1038 Å equivalent widths would then be 1.5–2 times this value in the optically thin and thick limits, respectively, which yields a range of 0.3–2.6 Å or 0.4–3.4 Å. The measured full widths at half-maximum of the O VI lines in this sample are 118–763  $\text{km s}^{-1}$ . We verified that these line widths correlate with the equivalent widths, much as they correlate with the column densities (T. M. Heckman et al. 2002; J. P. Grimes et al. 2009; R. Bordoloi et al. 2017). The [O II] line widths in Makani average  $\langle \text{FWHM} \rangle = 900 \text{ km s}^{-1}$  in the inner wind (D. S. N. Rupke et al. 2023). Assuming that the O VI line widths are at least as large, then we might expect an equivalent width of order 4–5 Å. Scaling from the line width, the corresponding absorption column density is  $\log(N_{\text{O VI}}/\text{cm}^{-2}) \sim 15.3$ , or 4 times higher than in J1156 (M. Hayes et al. 2016).

The similarity of these estimates of absorption and emission equivalent width toward the starlight suggests that any O VI emission interior to  $\sim 1''$  is offset by corresponding absorption. The other  $\sim 85\%$  of the O VI we observe in emission is then due to in situ processes and not dominated by scattering. However, this simple scenario could be modified by dust that blocks back-scattered O VI toward the nucleus and reduces redshifted emission or, alternatively, by the fact that we observe the starlight along a low-column-density sight line that reduces blueshifted absorption (J. X. Prochaska et al. 2011).

Resonant emission is observed in Makani in Na I D and Mg II, which are much lower ionization states (D. S. N. Rupke et al. 2019, 2023). The Na I D absorption and emission equivalent widths are approximately equal in magnitude, at a relatively small 0.4–0.5 Å in the central arcsecond (D. S. N. Rupke et al. 2023). There is no detectable Mg II absorption. However, both doublets show emission out to 10–20 kpc. If the emission from these lines is due to continuum scattering, then perhaps such scattering in these ions is not compensated for by line-of-sight absorption due to spherical asymmetry. However, this extended emission may also be line scattering from collisional excitation or photo-ionization (A. Henry et al. 2018; J. Chisholm et al. 2020). Relatedly, large-scale galaxy formation simulations suggest line scattering could dominate X-ray emission lines from higher ionization states like O VII in high-mass galaxies beyond 100 kpc (D. Nelson et al. 2023).

### 4.3. Cool Clouds in a Hot Wind

This basic morphology implies that most of the O VI we observe arises not from the hot, volume-filling CGM, but rather from the interaction between cool,  $T \approx 10^4 \text{ K}$  clouds and the hot,  $T > 10^6 \text{ K}$  haloes in which they are embedded (T. M. Heckman et al. 2001; J. Chisholm et al. 2018;

D. B. Fielding & G. L. Bryan 2022). This interaction causes hydrodynamic instabilities (e.g., E. Scannapieco & M. Brüggén 2015), which in turn produce turbulent mixing layers (e.g., M. Gronke & S. P. Oh 2018) that emit high-ionization UV lines in the interface between the hot and cool gas (e.g., J. D. Slavin et al. 1993). The clouds can grow as mass is transferred from the hot to the cool phase (M. Gronke & S. P. Oh 2018; D. B. Fielding et al. 2020). The gas cools radiatively, producing O VI as the temperature passes through  $T \approx 10^{5.5} \text{ K}$ . The emissivity of O VI peaks at this temperature in collisional ionization equilibrium (R. S. Sutherland & M. A. Dopita 1993).

Conversely, mass transfer can also move in the other direction. The cold clouds are heated through, for example, thermal conduction, and then mass loaded into the hot, surrounding medium. This arises in the interface between the  $10^7 \text{ K}$  wind fluid and entrained clouds in the launching region of a galactic wind. This leaves a signature in the X-ray-emitting wind fluid (D. K. Strickland & T. M. Heckman 2009). It also produces velocity stratification, in that higher-velocity gas is more highly ionized as evaporation proceeds under cloud acceleration (T. M. Heckman et al. 2001; J. P. Grimes et al. 2009; J. Chisholm et al. 2018).

As an example of how this emission may arise in large-scale winds as they propagate into the CGM, we show in Figure 13 the projected O VI emission from the simulations of M. Li & S. Tonnesen (2020). These simulations include mass loading into the hot wind from cloud evaporation at small scales (M. Li et al. 2017b). As the hot wind expands into the CGM, the hot halo gas “saturates” and cool clouds condense from the hot gas in clumpy, filamentary structures. The simulations shown are for winds produced by a  $6 \times 10^{10} M_{\odot}$  galaxy, which is 50%–100% of the mass of Makani (D. S. N. Rupke et al. 2019; K. E. Whalen et al. 2022). The SFRs of the two simulations are  $30 M_{\odot} \text{ yr}^{-1}$  and  $200 M_{\odot} \text{ yr}^{-1}$ , or 10% and 70% of the time-averaged SFR of Makani (G. C. Petter et al. 2020). The filamentary structure of O VI is similar to that observed in Makani (Figure 10), including the scale of the emission and the observed fluxes. In this model, the hot, outflowing wind is critical for the formation of the cool clouds observed in [O II], which also emit in O VI at the same physical location as the gas radiatively cools. Other high-resolution, global galaxy simulations also find that cool cloud mixing with the hot phase is an important acceleration mechanism for the wind, further implicating this process (E. E. Schneider et al. 2020).

As another example, large-scale cosmological simulations produce outflow structures that strongly resemble the morphology and scale of the Makani wind (D. Nelson et al. 2019; A. Pillepich et al. 2021). These structures produce in situ emission lines from highly ionized gas in ionization equilibrium (D. Nelson et al. 2023), like those observed in Makani from O VI.

### 4.4. Shock Models

Alternatively, the O VI emission could arise from shock ionization as the wind propagates through the CGM. In D. S. N. Rupke et al. (2023), we argued that the warm ionized gas observed in strong, rest-frame optical lines is consistent with shock models. This conclusion was based a comparison of line ratios and kinematics to the predictions of M. G. Allen et al. (2008). These models point to preshock densities in the range  $n_{\text{H}} = 1$  to  $10 \text{ cm}^{-3}$ , with postshock densities rising to

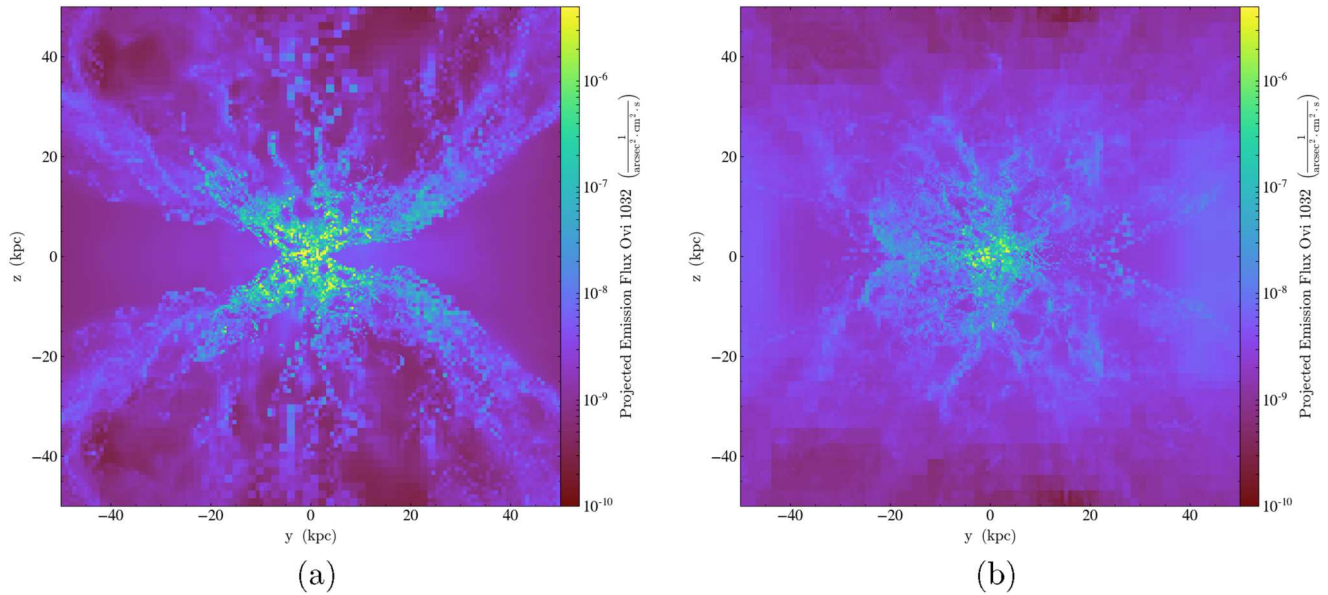


**Figure 13.** Projected O VI 1032 Å emission from the simulations of M. Li & S. Tonnesen (2020). Shown is a  $6 \times 10^{10} M_{\odot}$  galaxy with an SFR of (a)  $30 M_{\odot} \text{ yr}^{-1}$  and (b)  $200 M_{\odot} \text{ yr}^{-1}$ . The units are  $\text{photon s}^{-1} \text{ cm}^{-2} \text{ arcsec}^{-2}$ . Assuming similar emission from both doublet lines and reducing the simulated surface brightness to the redshift of Makani by  $(1+z)^4$ ,  $1 \times 10^{-6} \text{ photon s}^{-1} \text{ cm}^{-2} \text{ arcsec}^{-2} = 1 \times 10^{-17} \text{ erg s}^{-1} \text{ cm}^{-2} \text{ arcsec}^{-2}$ . The scale and brightness of the filamentary structure are similar to those observed in Makani (Figure 10). In this model, O VI arises primarily from the condensation of the hot CGM into cool clouds as a hot wind blows into the CGM.

$n_{\text{H}} = 600 \text{ cm}^{-3}$  to  $6000 \text{ cm}^{-3}$ . The larger densities apply to the inner ( $r \lesssim 15 \text{ kpc}$ ) episode II wind with  $\langle \sigma \rangle = 400 \text{ km s}^{-1}$ . The smaller apply to the outer, older episode I wind with  $\langle \sigma \rangle = 200 \text{ km s}^{-1}$ .

These same models predict fluxes for both O VI and Ly $\alpha$ . In Section 3.3 we compute the flux ratios O VI/Ly $\alpha$  and [O II]/O VI. In Figure 14 we compare the observed ratios to model predictions. We show shock+precursor models with solar and Large Magellanic Cloud (LMC) abundances and with densities  $n = 1 \text{ cm}^{-3}$  and  $100 \text{ cm}^{-3}$ , corresponding to models M, Q, and L of M. G. Allen et al. (2008). We vary the model grids over magnetic parameter  $b \equiv Bn^{-1/2}$  and shock velocity.

In comparing to the shock models, we also consider a correction for attenuation. The optical recombination lines are consistent with a range of attenuation values  $E(B-V) = 0.3\text{--}1.0 \text{ mag}$  at  $r \lesssim 20 \text{ kpc}$  and no attenuation at larger radius (D. S. N. Rupke et al. 2023). If these apply also to the observed UV lines, then even small amounts of attenuation can change the ratios in Figure 14. Using the `dust_extinction` package (K. D. Gordon 2024), we display the magnitude of a fiducial correction using the K. D. Gordon et al. (2023) models,  $R_V = 3.1$ , and a modest  $E(B-V) = 0.3 \text{ mag}$  of attenuation. This would apply only to bins with  $r < 20 \text{ kpc}$ . We caution that the extinction correction is quite uncertain, and this is exercise is intended mainly to illustrate the possible impact of extinction.

The solar abundance  $n = 1 \text{ cm}^{-3}$  model does not overlap the data, as it does for the optical ratios in the outer wind (D. S. N. Rupke et al. 2023). A lower, LMC-like abundance is potentially consistent with the data if there is no extinction. A lower abundance may be consistent with absorbers in the CGM, which point to  $\langle Z \rangle = Z_{\odot}/3$  at  $z \approx 0.2$  (J. X. Prochaska et al. 2017). The inner,  $r < 30 \text{ kpc}$  bins overlap with the  $400 \text{ km s}^{-1}$  models, which are the best fit to the optical-line ratios in this part of the nebula (D. S. N. Rupke et al. 2023). The outer bins are consistent with  $300 \text{ km s}^{-1}$ , while the best-fit models in the optical are closer to  $\approx 200 \text{ km s}^{-1}$ . However,

in the presence of extinction, the inner points move outside of the model grids. Increasing the density to  $100 \text{ cm}^{-3}$ , rather than decreasing the abundances, yields a match to the inner, attenuation-corrected data. However, the observed data (uncorrected for attenuation) are then only compatible with shock velocity  $> 500 \text{ km s}^{-1}$ .

In summary, the lower-metallicity shock models are the best overall match to the data, but only in the absence of extinction. It is conceivable that [O II] and O VI experience different levels of extinction, particularly if they arise at different layers within a cloud in the shock. For instance, if [O II] arises further into the cloud interior, then it could experience higher extinction. Correcting for this will raise, rather than lower, the [O II]/O VI ratio. The attenuation correction is also sensitive to the exact values of  $E(B-V)$ , which has limited spatial constraints; the choice of extinction curve; and the choice of  $R_V$ . There may also be differences arising due to large-scale geometry (see below).

A second uncertainty is the susceptibility of Ly $\alpha$  to radiative transfer effects. The shock models assume the Ly $\alpha$  line is emitted from the same volume as other lines. However, Ly $\alpha$  is emitted from starburst production sites in the galaxy and, if it escapes, scatters off the wind. In J1156, the Ly $\alpha$  nebula is much more compact than the O VI halo and may arise due to scattering (M. Hayes et al. 2016). In contrast, we show above that the data for Makani are consistent with a Ly $\alpha$  nebula of the same morphology as O VI. If Ly $\alpha$  is at least in part due to scattering, then removing this contribution from the data would raise the O VI/Ly $\alpha$  ratio of emission attributable to in situ processes, like shock ionization. This would improve the match to the shock models.

For comparison, O VI emission has been observed spectroscopically in the AGN-driven outflow surrounding a  $z = 0.123$  quasar (J. Somalwar et al. 2020). The ionization of the gas in the nucleus and at  $10 \text{ kpc}$  radius produces O VI/Ly $\alpha = 0.2$ , which is identical to what we observe in the Makani wind. In this case, the wind is AGN photoionized, which is not the case

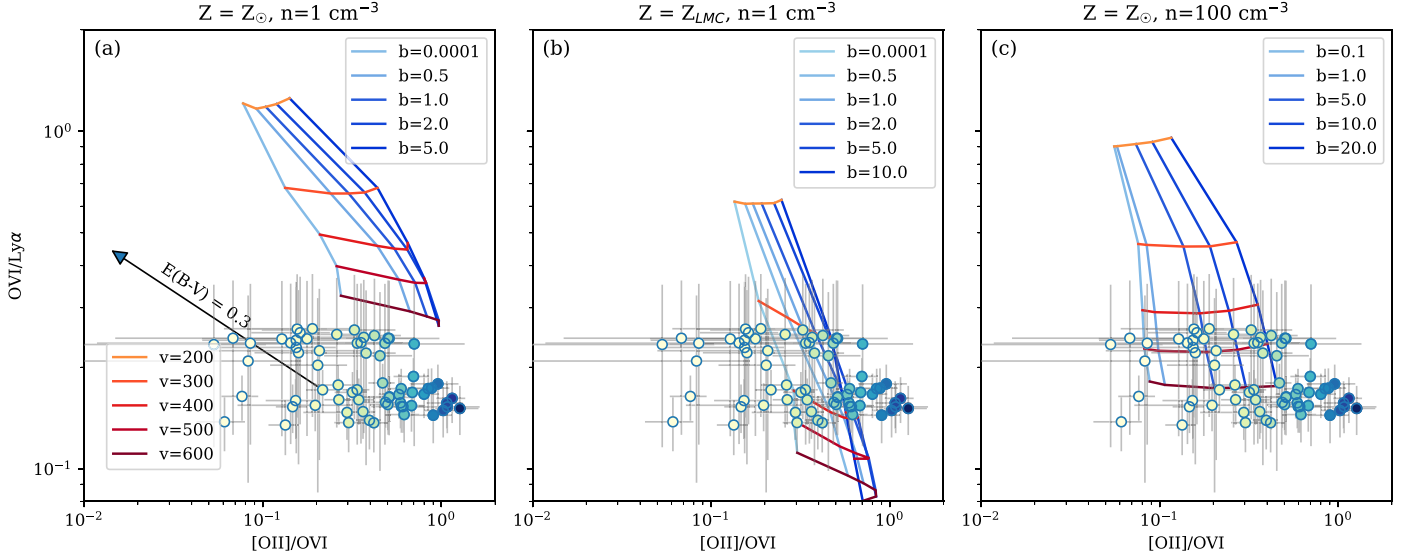


**Figure 14.** Line ratios vs. shock model predictions. (a) Solar metallicity,  $n = 1 \text{ cm}^{-3}$  grids (M. G. Allen et al. 2008). (b) LMC metallicity,  $n = 1 \text{ cm}^{-3}$  grids. (c) Solar metallicity,  $n = 100 \text{ cm}^{-3}$  grids.  $[\text{O II}] 3727, 3729 \text{ \AA}/\text{O VI } 1032, 1038 \text{ \AA}$  ratios represent individual Voronoi bins (Figure 11(a)). The  $\text{O VI}/\text{Ly}\alpha$  ratios for each point correspond to one of two average values calculated in radial bins (Figure 7 and Section 3.3); we have also added a small vertical random scatter to each point for display purposes. Error bars are  $1\sigma$ . With the arrow, we show the effect of  $E(B - V) = 0.3$  mag, which is the minimum observed extinction at radii  $r < 20$  kpc with optical recombination lines (D. S. N. Rupke et al. 2023). Colors represent  $[\text{O II}]/\text{O VI}$ , as in Figure 11(b). The model grids show a range of magnetic parameter  $b \equiv Bn^{-1/2}$  in units of  $\mu\text{G cm}^{-3/2}$  and shock velocity in  $\text{km s}^{-1}$ . LMC models provide the best fit to the observed ratios, although this conclusion could change in the presence of attenuation.

for Makani, since it has no detectable AGN (P. H. Sell et al. 2014; D. S. N. Rupke et al. 2019).

If the UV lines require an ionization mechanism other than shocks, then the morphology of the line ratios offers a clue to their origin. The map of  $[\text{O II}]/\text{O VI}$  (Figure 11(a)) shows that the highest values are found in the east and west high-surface-brightness regions of the nebula, at the bases of the lobes of the hourglass shape. The lowest values are found directly north and south of the nucleus and in the most extended regions of the nebula. In a scenario where the hourglass is a container for a hot wind fluid that propagates primarily north and south, then the lower values of  $[\text{O II}]/\text{O VI}$  along this “channel” could trace ionization of the gas through interaction with this fluid (T. M. Heckman et al. 2001; J. Chisholm et al. 2018). As an example of another ionization mechanism, models of turbulent mixing layers in cloud/wind interfaces predict  $[\text{O II}]/\text{O VI} \gtrsim 10$  (J. D. Slavin et al. 1993; Z. Chen et al. 2023). These values are significantly higher than observed but could be compatible with the data if the  $[\text{O II}]$  lines are preferentially attenuated. Finally, flickering AGNs can also ionize  $\text{O VI}$ , which then recombines within  $10^7$  yr, well after lower-ionization species (B. D. Oppenheimer et al. 2018).

Alternatively, these morphological differences may represent differences in extinction. If the east and west regions have higher extinction—as possibly indicated by the dense gas observed in these directions through CO measurements (D. S. N. Rupke et al. 2019)—then  $\text{O VI}$  would be suppressed in these regions compared to  $[\text{O II}]$ , raising the observed  $[\text{O II}]/\text{O VI}$ . As pointed out by J.-A. Kim et al. (2024), this difference in optical depth may impact which part of the wind is probed by each line, if it also reflects a difference in geometric depth.

#### 4.5. Mass and Density

The typical mass of  $\text{O VI}$  in the CGM of a galaxy with  $M_* = 10^{11} M_\odot$  is  $M_{\text{O VI}} \approx 3 \times 10^6 M_\odot$  (K. Tchernyshyov et al. 2022). Using this ensemble measurement—and making the

assumption that the  $\text{O VI}$  observed in Makani dominates the estimated mass budget of  $\text{O VI}$  within the virial radius—we estimate the density in the  $\text{O VI}$  nebula of Makani. The  $\text{O VI}$  volume emission rate is equal to the volumetric cooling rate in  $\text{O VI}$ ,  $\Lambda_{\text{O VI}}$  (R. S. Sutherland & M. A. Dopita 1993). Following M. Hayes et al. (2016), we adopt the solar metallicity value of  $\Lambda_{\text{O VI}}$  from S. Bertone et al. (2010),  $\Lambda_{\text{O VI}}^Z = (5 \times 10^{-23} \text{ erg s}^{-1} \text{ cm}^{-3}) n_e^2$ , and scale by  $Z$ :  $\Lambda_{\text{O VI}} = \Lambda_{\text{O VI}}^Z (Z/Z_\odot)$ . The mass and luminosity are then related as

$$M_{\text{O VI}} = \rho_{\text{O VI}} L_{\text{O VI}} \Lambda_{\text{O VI}}^{-1} \quad (8)$$

$$= 16m_p n_e (N_{\text{O}}/N_{\text{H}}) L_{\text{O VI}} [\Lambda_{\text{O VI}}^Z (Z/Z_\odot)]^{-1} \quad (9)$$

$$= (1.32 \times 10^5 M_\odot) \left( \frac{L_{\text{O VI}}}{10^{42} \text{ erg s}^{-1}} \right) \left( \frac{1 \text{ cm}^{-3}}{n_e} \right) \left( \frac{Z_\odot}{Z} \right). \quad (10)$$

Here,  $\rho_{\text{O VI}}$  is the mass density of  $\text{O VI}$  atoms. We assume that the plasma is completely ionized and that  $\text{O VI}$  dominates the oxygen budget during the  $10^{5.5}$  K phase, which means  $n_{\text{O VI}} \approx n_e (N_{\text{O}}/N_{\text{H}})$ . We adopt the solar oxygen abundance of M. Asplund et al. (2021).

From Equation (10), the observed  $\text{O VI}$  luminosity in Makani is then equivalent to the ensemble halo mass at a density of  $n_e = 0.5 \text{ cm}^{-3}$ , assuming a metallicity of  $Z_\odot/3$  (J. X. Prochaska et al. 2017). This value is identical to that inferred for the J1156 nebula (M. Hayes et al. 2016). It is similar to the density of the warm, ionized, preshock gas in the outer parts of the Makani wind, as inferred from shock models (D. S. N. Rupke et al. 2023). The preshock density inferred for the inner wind is about 10 times higher. Correcting for possible extinction would raise the inferred density proportionally.

Although we do not measure density  $n$  or column density  $N$  directly, our estimates for the two are roughly consistent. Since luminosity  $L \propto n^2 V$  and  $N \propto nL$ —where  $V$  is the emitting volume and  $L$  is the path length—then  $L/N \propto nV/L \sim nA$ , where  $A$  is the area of a cross section of the emitting volume.

Comparing to J1156,  $L$  in Makani is 20 times higher (Section 4.1), while our  $N$  estimate is only 4 times bigger (Section 4.2), so that  $(L/N)_{\text{Makani}} = 5(L/N)_{\text{J1156}}$ . The estimated densities of the two sources are the same, while the area  $A$  of Makani’s nebula is larger than that of J1156 by the ratio of their half-light radii squared,  $(20/12.6)^2 \sim 2.5$ . Thus,  $(nA)_{\text{Makani}} = 2.5(nA)_{\text{J1156}}$ . The two sides of the equation are thus consistent within a factor of 2, which is reasonable given the uncertainties and assumptions.

Finally, we note that the cooling time of O VI is  $t_{\text{cool}} \approx 1$  Myr (O. Gnat & A. Sternberg 2007). If the ensemble O VI mass applies to Makani, and O VI represents gas condensing from the hot to the cold phase, then the predicted total oxygen cooling rate in the Makani wind is  $\dot{M}_{\text{cool}}^{\text{OVI}} = M_{\text{O VI}}/t_{\text{cool}} \approx 3 M_{\odot} \text{ yr}^{-1}$ . The total predicted cooling rate in the nebula is then  $\dot{M}_{\text{cool}} \approx 1500 M_{\odot} \text{ yr}^{-1}$ , for  $Z = Z_{\odot}/3$ . If a quarter of this cooling is in the inner wind, scaling by the relative flux of the inner exponential, then the cooling rate at  $r \lesssim 15$  kpc is comparable to the mass outflow rate of the fast, inner wind (D. S. N. Rupke et al. 2023). However, the remaining cooling rate is two orders of magnitude greater than that in the slow, outer wind (D. S. N. Rupke et al. 2023). This points to the possibility of the increased importance of cooling versus mass outflow for the cloud mass budget as the wind ages, slows, and moves to larger radius.

## 5. Conclusions

The galaxy Makani is a compact, massive ( $M_* \sim 10^{11} M_{\odot}$ ) galaxy observed at a look-back time of 4.6 Gyr (P. H. Sell et al. 2014). It hosts a 100 kpc outflow detected in [O II] using ground-based integral field spectroscopy with KCWI (D. S. N. Rupke et al. 2019). This  $\sim 10^{10} M_{\odot}$  outflow has been produced over 400 Myr through two strong starburst events (D. S. N. Rupke et al. 2019). The warm, ionized line-emitting nebula is consistent with shock excitation and powering by a momentum-conserving flow from the starburst (D. S. N. Rupke et al. 2023).

Using the narrowband filters of the ACS-SBC on HST, we have performed 20 orbits of deep imaging to produce F150LP and F165LP images of Makani. We have shown that there is significant, extended emission in F150LP and F165LP that arises primarily from O VI+ Ly $\alpha$  and Ly $\alpha$  emission, respectively. This extended emission is significantly detected at radii  $\approx 1''$  to  $5''$  in F165LP and  $\approx 1''$  to  $8''$  in F150LP. Based on an analysis of the noise in the F165LP image, we infer that it is also consistent with the more extended emission observed in F150LP. This corresponds to a UV line-emitting nebula over projected radii of 10–50 kpc.

Using Voronoi binning and the F165LP image to separate O VI and Ly $\alpha$ , we produce an O VI image that strongly resembles the hourglass morphology of the [O II] emission observed in Makani. The [O II]/O VI and O VI/Ly $\alpha$  line ratios are potentially consistent with shock models (M. G. Allen et al. 2008), with the caveats that attenuation and radiative transfer effects on Ly $\alpha$  are uncertain. Turbulent mixing layer models (e.g., Z. Chen et al. 2023) predict [O II]/O VI ratios higher than observed. However, the spatial coincidence of the [O II] and O VI gas strongly implies that the latter arises in the interface between a hot,  $10^7$  K phase—the ambient CGM and/or the fluid driving the wind—and cool clouds. The O VI arises as gas cools from a hot phase, perhaps contributing to in situ cloud

growth. The morphology of the O VI outflow is consistent with models and simulations of gas cooling in a hot wind.

The halo or CGM of only one other galaxy has been imaged in O VI. Makani has an SFR 10 times that of J1156 (M. Hayes et al. 2016), and its  $L_{\text{O VI}} \approx 4 \times 10^{42} \text{ erg s}^{-1}$  is correspondingly larger. The O VI emission in Makani extends  $\gtrsim 2$  times as far as that in J1156 and has a double-exponential—rather than single-exponential in J1156—radial profile. Nonetheless, the estimated density in the O VI-emitting phase,  $n_e \approx 0.5 \text{ cm}^{-3}$ , may be similar. Spectroscopy of O VI in Makani would, in combination with the imaging data, better constrain the density and inner structure of the wind, as well as the kinematics of the coronal gas and possible scattering geometries.

This experiment represents the bleeding edge of the UV imaging capability of HST for detecting emission in the CGM of galaxies. A future, large-area, UV space-based mission with narrowband imaging capability or integral field spectroscopy—such as the Habitable World Observatory—will be poised to detect such signals in larger samples of galaxies (The LUVOIR Team 2019). Along with the previous detection in J1156, we have shown that detecting cooling gas, which primarily emits in UV line emission (S. Bertone et al. 2013), may be easier than expected if galactic winds enhance the detectability of such lines. Natural future targets might be the ubiquitous [O II] nebula surrounding  $z < 1$  quasars (S. D. Johnson et al. 2024).

## Acknowledgments

We thank Sally Heap for the idea to apply the differential narrowband technique to Makani. We thank Matthew Hayes for sharing data on J1156 and for other helpful conversations on the analysis. This research is based on observations made with the NASA/ESA Hubble Space Telescope obtained from the Space Telescope Science Institute, which is operated by the Association of Universities for Research in Astronomy, Inc., under NASA contract NAS 5-26555. These observations are associated with program #16231. Support for program #16231 was provided by NASA through a grant from the Space Telescope Science Institute.

*Facility:* HST (ACS-SBC).

*Software:* *astropy* (Astropy Collaboration et al. 2013, 2018, 2022), *DrizzlePac* (STScI Development Team 2012), *dust\_extinction* (K. D. Gordon 2024), *photutils* (L. Bradley et al. 2024a), *regions* (L. Bradley et al. 2024b), *reproject* (T. Robitaille et al. 2020), *stsynphot* (STScI Development Team 2020), *synphot* (STScI Development Team 2018), *VorBin* (M. Cappellari & Y. Copin 2003).

## ORCID iDs

Triet Ha  <https://orcid.org/0009-0000-3788-9059>  
 David S. N. Rupke  <https://orcid.org/0000-0002-1608-7564>  
 Alison L. Coil  <https://orcid.org/0000-0002-2583-5894>  
 Miao Li  <https://orcid.org/0000-0003-0773-582X>  
 Christy A. Tremonti  <https://orcid.org/0000-0003-3097-5178>  
 Ryan C. Hickox  <https://orcid.org/0000-0003-1468-9526>  
 Sean D. Johnson  <https://orcid.org/0000-0001-9487-8583>  
 Gene C. K. Leung  <https://orcid.org/0000-0002-9393-6507>  
 John Moustakas  <https://orcid.org/0000-0002-2733-4559>  
 Serena Perrotta  <https://orcid.org/0000-0002-2451-9160>  
 Gregory H. Rudnick  <https://orcid.org/0000-0001-5851-1856>  
 Paul H. Sell  <https://orcid.org/0000-0003-1771-5531>  
 Kelly E. Whalen  <https://orcid.org/0000-0002-8571-9801>

## References

- Allen, M. G., Groves, B. A., Dopita, M. A., Sutherland, R. S., & Kewley, L. J. 2008, *ApJS*, **178**, 20
- Asplund, M., Amarsi, A. M., & Grevesse, N. 2021, *A&A*, **653**, A141
- Astropy Collaboration, Price-Whelan, A. M., Lim, P. L., et al. 2022, *ApJ*, **935**, 167
- Astropy Collaboration, Price-Whelan, A. M., Sipőcz, B. M., et al. 2018, *AJ*, **156**, 123
- Astropy Collaboration, Robitaille, T. P., Tollerud, E. J., et al. 2013, *A&A*, **558**, A33
- Avila, R. J. 2017, Updated Measurements of ACS/SBC Dark Rates, Instrument Science Report ACS 2017-4, STScI 8
- Avila, R. J., Arslanian, S., Bourque, M., & Eck, W. 2018, Mitigating Elevated Dark Rates in SBC Imaging, Instrument Science Report ACS 2018-07, STScI 6
- Avila, R. J., & Chiaberge, M. 2016, Photometric Aperture Corrections for the ACS/SBC, Instrument Science Report ACS 2016-5, STScI 8
- Bertone, S., Aguirre, A., & Schaye, J. 2013, *MNRAS*, **430**, 3292
- Bertone, S., Schaye, J., Booth, C. M., et al. 2010, *MNRAS*, **408**, 1120
- Bordoloi, R., Wagner, A. Y., Heckman, T. M., & Norman, C. A. 2017, *ApJ*, **848**, 122
- Bradley, L., Deil, C., Ginsburg, A., et al. 2024b, *astropy/regions*: v0.10, Zenodo, doi:10.5281/zenodo.13852178
- Bradley, L., Sipőcz, B., Robitaille, T., et al. 2024a, *astropy/photutils*: v2.0.2, Zenodo, doi:10.5281/zenodo.13989456
- Brown, R. L., & Mathews, W. G. 1970, *ApJ*, **160**, 939
- Cappellari, M., & Copin, Y. 2003, *MNRAS*, **342**, 345
- Chen, Z., Fielding, D. B., & Bryan, G. L. 2023, *ApJ*, **950**, 91
- Chisholm, J., Bordoloi, R., Rigby, J. R., & Bayliss, M. 2018, *MNRAS*, **474**, 1688
- Chisholm, J., Prochaska, J. X., Schaerer, D., Gazagnes, S., & Henry, A. 2020, *MNRAS*, **498**, 2554
- Cox, C. 2009, Re-measurement of ACS/SBC dark images, Instrument Science Report ACS 2009-02, STScI 7
- Davis, J. D., Tremonti, C. A., Swiggum, C. N., et al. 2023, *ApJ*, **951**, 105
- Dey, A., Schlegel, D. J., Lang, D., et al. 2019, *AJ*, **157**, 168
- Diamond-Stanic, A. M., Moustakas, J., Sell, P. H., et al. 2021, *ApJ*, **912**, 11
- Diamond-Stanic, A. M., Moustakas, J., Tremonti, C. A., et al. 2012, *ApJL*, **755**, L26
- Dijkstra, M. 2009, *ApJ*, **690**, 82
- Draine, B. T. 2003, *ApJ*, **598**, 1017
- Fielding, D. B., & Bryan, G. L. 2022, *ApJ*, **924**, 82
- Fielding, D. B., Tonnesen, S., DeFelippis, D., et al. 2020, *ApJ*, **903**, 32
- Foreman-Mackey, D., Hogg, D. W., Lang, D., & Goodman, J. 2013, *PASP*, **125**, 306
- Gnat, O., & Sternberg, A. 2007, *ApJS*, **168**, 213
- Gordon, K. D. 2024, *JOSS*, **9**, 7023
- Gordon, K. D., Clayton, G. C., Declair, M., et al. 2023, *ApJ*, **950**, 86
- Grimes, J. P., Heckman, T., Aloisi, A., et al. 2009, *ApJS*, **181**, 272
- Grimes, J. P., Heckman, T., Strickland, D., et al. 2007, *ApJ*, **668**, 891
- Gronke, M., & Oh, S. P. 2018, *MNRAS*, **480**, L111
- Guzman, A. M., & Avila, R. J. 2024, Updates to the SBC Dark Rate Monitor, Instrument Science Report ACS 2024-04, STScI 15
- Hafen, Z., Faucher-Giguère, C.-A., Anglés-Alcázar, D., et al. 2019, *MNRAS*, **488**, 1248
- Hayes, M., Melinder, J., Östlin, G., et al. 2016, *ApJ*, **828**, 49
- Heckman, T. M., Borthakur, S., Overzier, R., et al. 2011, *ApJ*, **730**, 5
- Heckman, T. M., Norman, C. A., Strickland, D. K., & Sembach, K. R. 2002, *ApJ*, **577**, 691
- Heckman, T. M., Sembach, K. R., Meurer, G. R., et al. 2001, *ApJ*, **554**, 1021
- Henry, A., Berg, D. A., Scarlata, C., Verhamme, A., & Erb, D. 2018, *ApJ*, **855**, 96
- Henry, A., Scarlata, C., Martin, C. L., & Erb, D. 2015, *ApJ*, **809**, 19
- Hodges-Kluck, E., Cafmeyer, J., & Bregman, J. N. 2016, *ApJ*, **833**, 58
- Hoopes, C. G., Heckman, T. M., Strickland, D. K., et al. 2005, *ApJL*, **619**, L99
- Johnson, S. D., Liu, Z. W., Li, J. I. H., et al. 2024, *ApJ*, **966**, 218
- Kim, J.-A., Chung, H., Vargas, C. J., & Hamden, E. 2024, *AJ*, **168**, 11
- Lang, D., Hogg, D. W., & Mykytyn, D. 2016, The Tractor: Probabilistic Astronomical Source Detection and Measurement, Astrophysics Source Code Library, ascl:1604.008
- Lehmann, A., Godard, B., Pineau des Forêts, G., & Falgarone, E. 2020, *A&A*, **643**, A101
- Li, M., Bryan, G. L., & Ostriker, J. P. 2017a, *ApJL*, **835**, L10
- Li, M., Bryan, G. L., & Ostriker, J. P. 2017b, *ApJ*, **841**, 101
- Li, M., & Tonnesen, S. 2020, *ApJ*, **898**, 148
- Lucas, R. A., Ryon, J. E., et al. 2022, ACS Data Handbook v. 11.0 (Baltimore: STScI)
- Meléndez, M., Veilleux, S., Martin, C., et al. 2015, *ApJ*, **804**, 46
- Morton, D. C. 1991, *ApJS*, **77**, 119
- Nelson, D., Byrohl, C., Ogorzalek, A., et al. 2023, *MNRAS*, **522**, 3665
- Nelson, D., Pillepich, A., Springel, V., et al. 2019, *MNRAS*, **490**, 3234
- Newville, M., Otten, R., Nelson, A., et al. 2024, *lmfit/lmfit-py*: v1.3.2, Zenodo, doi:10.5281/zenodo.598352
- Nussbaumer, H., & Schmutz, W. 1984, *A&A*, **138**, 495
- Oppenheimer, B. D., Crain, R. A., Schaye, J., et al. 2016, *MNRAS*, **460**, 2157
- Oppenheimer, B. D., Segers, M., Schaye, J., Richings, A. J., & Crain, R. A. 2018, *MNRAS*, **474**, 4740
- Otte, B., Murphy, E. M., Howk, J. C., et al. 2003, *ApJ*, **591**, 821
- Ouchi, M., Ono, Y., & Shibuya, T. 2020, *ARA&A*, **58**, 617
- Perrotta, S., Coil, A. L., Rupke, D. S. N., et al. 2023, *ApJ*, **949**, 9
- Perrotta, S., George, E. R., Coil, A. L., et al. 2021, *ApJ*, **923**, 275
- Petter, G. C., Kepley, A. A., Hickox, R. C., et al. 2020, *ApJ*, **901**, 138
- Pillepich, A., Nelson, D., Truong, N., et al. 2021, *MNRAS*, **508**, 4667
- Planck Collaboration, Aghanim, N., Akrami, Y., et al. 2020, *A&A*, **641**, A6
- Prochaska, J. X., Kasen, D., & Rubin, K. 2011, *ApJ*, **734**, 24
- Prochaska, J. X., Werk, J. K., Worseck, G., et al. 2017, *ApJ*, **837**, 169
- Robertson, J. G. 1986, *PASP*, **98**, 1220
- Robitaille, T., Deil, C., & Ginsburg, A. 2020, reproject: Python-based Astronomical Image Reprojection, Astrophysics Source Code Library, ascl:2011.023
- Rupke, D. S. N., Coil, A., Geach, J. E., et al. 2019, *Natur*, **574**, 643
- Rupke, D. S. N., Coil, A. L., Perrotta, S., et al. 2023, *ApJ*, **947**, 33
- Ryon, J. E., Stark, D. V., et al. 2023, ACS Instrument Handbook, Version 23.0 (Baltimore: STScI)
- Scannapieco, E., & Brügggen, M. 2015, *ApJ*, **805**, 158
- Scarrott, S. M., Eaton, N., & Axon, D. J. 1991, *MNRAS*, **252**, 12P
- Schneider, E. E., Ostriker, E. C., Robertson, B. E., & Thompson, T. A. 2020, *ApJ*, **895**, 43
- Sell, P. H., Tremonti, C. A., Hickox, R. C., et al. 2014, *MNRAS*, **441**, 3417
- Sirianni, M., Jee, M. J., Benítez, N., et al. 2005, *PASP*, **117**, 1049
- Slavin, J. D., Shull, J. M., & Begelman, M. C. 1993, *ApJ*, **407**, 83
- Somalwar, J., Johnson, S. D., Stern, J., et al. 2020, *ApJL*, **890**, L28
- Strickland, D. K., & Heckman, T. M. 2009, *ApJ*, **697**, 2030
- STScI Development Team 2012, DrizzlePac: HST Image Software, Astrophysics Source Code Library, ascl:1212.011
- STScI Development Team 2018, synphot: Synthetic Photometry Using Astropy, Astrophysics Source Code Library, ascl:1811.001
- STScI Development Team 2020, stsynphot: Synphot for HST and JWST, Astrophysics Source Code Library, ascl:2010.003
- Sutherland, R. S., & Dopita, M. A. 1993, *ApJS*, **88**, 253
- Tchernyshyov, K., Werk, J. K., Wilde, M. C., et al. 2022, *ApJ*, **927**, 147
- Tchernyshyov, K., Werk, J. K., Wilde, M. C., et al. 2023, *ApJ*, **949**, 41
- Teplitz, H. I., Siana, B., Brown, T. M., et al. 2006, *AJ*, **132**, 853
- The LUVOIR Team 2019, arXiv:1912.06219
- Tran, H. D., Meurer, G. R., Ford, H. C., et al. 2003, *Proc. SPIE*, **4854**, 686
- Tripp, T. M., Meiring, J. D., Prochaska, J. X., et al. 2011, *Sci*, **334**, 952
- Tumlinson, J., Thom, C., Werk, J. K., et al. 2011, *Sci*, **334**, 948
- Veilleux, S., Rupke, D. S. N., Liu, W., et al. 2022, *ApJ*, **926**, 60
- Veilleux, S., Shockey, S. S., Meléndez, M., et al. 2025, *ApJ*, submitted
- Verhamme, A., Schaerer, D., & Maselli, A. 2006, *A&A*, **460**, 397
- Werk, J. K., Prochaska, J. X., Tumlinson, J., et al. 2014, *ApJ*, **792**, 8
- Whalen, K. E., Hickox, R. C., Coil, A. L., et al. 2022, *AJ*, **164**, 222
- Zhou, R., Guy, J., Kposov, S. E., et al. 2024, arXiv:2409.05140